CHEMISTRY OF MATERIALS

Review

pubs.acs.org/cm

Imaging Impurities in Semiconductor Nanostructures

Vincent C. Holmberg,[†] Justin R. Helps,[‡] K. Andre Mkhoyan,[‡] and David J. Norris*[,†]

[†]Optical Materials Engineering Laboratory, ETH Zürich, 8092 Zürich, Switzerland

[‡]Department of Chemical Engineering and Materials Science, University of Minnesota, Minneapolis, Minnesota 55455, United States

ABSTRACT: Atomic impurities are critical for many technologies. They are used to engineer the optical and electronic properties of semiconductors for applications such as transistors, solar cells, light-emitting diodes (LEDs), and lasers, as well as to store energy for applications such as batteries and electrochemical cells. While the characterization and understanding of impurities in bulk semiconductors is well developed, new challenges arise at the nanoscale. In particular, methods are needed to characterize structures that may only contain a few impurity atoms. With such techniques, a fundamental understanding of how atomic impurities affect the properties of semiconductor nanostructures could be more fully developed. In this review, we give a brief introduction to the benefits and challenges associated with the incorporation of impurities in nanoscale structures, a process known as doping. We then focus on techniques used to characterize and image atomic impurities in semiconductor nanostructures. Advances in electron microscopy allow researchers to probe the dynamics of impurity incorporation with in situ transmission electron microscopy (TEM), and techniques such as electron energy loss spectroscopy (EELS) coupled with annular dark-field scanning transmission electron microscopy (ADF-STEM) allow individual atomic impurities in semiconductor nanostructures to be detected and imaged. Likewise, techniques such as atom probe tomography (APT) enable the full atomic reconstruction of nanoscale materials.

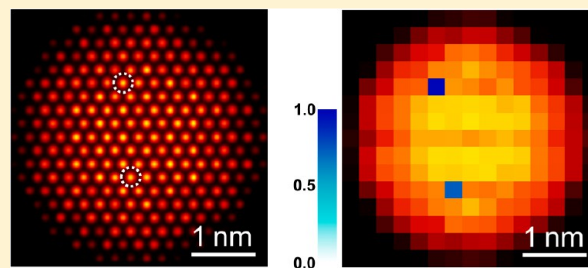

KEYWORDS: *electron energy loss spectroscopy, annular dark-field scanning transmission electron microscopy, in situ transmission electron microscopy, atom probe tomography, colloidal quantum dots, semiconductor nanocrystals, semiconductor nanowires, dopant imaging, impurity imaging, solotronics, doping*

I. INTRODUCTION

Semiconductors play a critical role in nearly all modern electronic devices, and for many decades scientists and engineers have worked to carefully control the physical properties of these materials. One of the main methods for modifying the behavior of semiconductors is to intentionally incorporate impurity atoms, also known as dopants. For example, electronically active impurities added to the semiconductor can donate extra electrons to the host lattice (*n*-type doping) or accept electrons from the host lattice, creating extra holes (*p*-type doping).[1] The presence of these excess charge carriers (electrons or holes, respectively) can then be used to tailor the electrical-transport properties of the semiconductor. Such dopants are central to the creation of transistors, solar cells, light-emitting diodes (LEDs), lasers, and many other devices.

Another method for controlling the physical properties of semiconductors is to change the size of the material. As observed over the last few decades, if the size of a semiconductor is reduced to nanoscale dimensions, dramatic effects can be observed in electrical,[2−4] optical,[5−7] and mechanical properties,[8] as well as in phase transitions[9−13] and diffusion.[13,14] In particular, when one or more of the dimensions of the material are smaller than the characteristic quantum-mechanical size of a carrier, the energy of the carrier can be tuned by altering the size of the small dimension.[15] This phenomenon, referred to as quantum confinement, has been a central concept in nanoscience. For example, carriers in thin planar layers of a semiconductor (known as quantum wells) experience confinement in one dimension and form the basis of many technologies such as laser diodes and photodetectors. Carriers in narrow semiconductor nanowires (known as quantum wires) experience confinement in two dimensions while maintaining freedom of motion along the axis of the wire, a characteristic that is useful for electrical transport. Carriers in small semiconductor nanocrystals (known as quantum dots) experience confinement in all three dimensions, which leads to materials with broadly tunable optical absorption and fluorescence, with applications ranging from solar cells to bioimaging.

However, as our understanding of the basic properties of nanostructures has developed, an obvious question is what happens when impurities are also added to these nanostructures.[16] In this case, one could potentially control properties both by incorporating dopants and by reducing the size of the

Special Issue: Synthetic and Mechanistic Advances in Nanocrystal Growth

Received: January 1, 2013
Revised: March 4, 2013
Published: March 5, 2013

 © 2013 American Chemical Society

material. Understanding this combination is also of practical importance as the actual size of semiconductor devices, which depend on dopants, continues to shrink. Furthermore, due to quantum confinement of the dopants, new physical phenomena can arise as the impurity is squeezed inside a small piece of semiconductor. Indeed, the emerging field of solotronics aims to utilize such effects in devices that contain a small number of dopant atoms within a semiconductor nanostructure.[17] Such devices are of interest, in part, due to the fact that confined impurities can lead to new optical, electrical, and magnetic behavior.

For example, the optical properties of colloidal quantum dots can be affected by the presence of dopants.[16] These particles, which are a few nanometers in diameter, have surfaces that are coated with surfactant molecules so that they can be easily dispersed in a liquid.[15] Pure nanocrystals (i.e., undoped) can exhibit fluorescence when photoexcited electrons and holes, which are confined in the particle, subsequently recombine. It is now well-known that the color of this emission can be altered if atomic impurities, such as Mn, are incorporated that can quickly capture the energy from the electron and hole before they recombine.[18−20] The impurity itself can then fluoresce via an atomic transition. More recently, it has also been shown that the incorporation of nonfluorescent, electronically active impurities (i.e., *n*- or *p*-type dopants) in colloidal quantum dots can alter the intensity of their fluorescence.[21,22] Figure 1 illustrates the influence of Ag impurities on the fluorescence of CdSe nanocrystals.[22] The addition of only 2−3 Ag atoms per nanocrystal causes an order-of-magnitude increase in the room temperature fluorescence efficiency from the semiconductor.

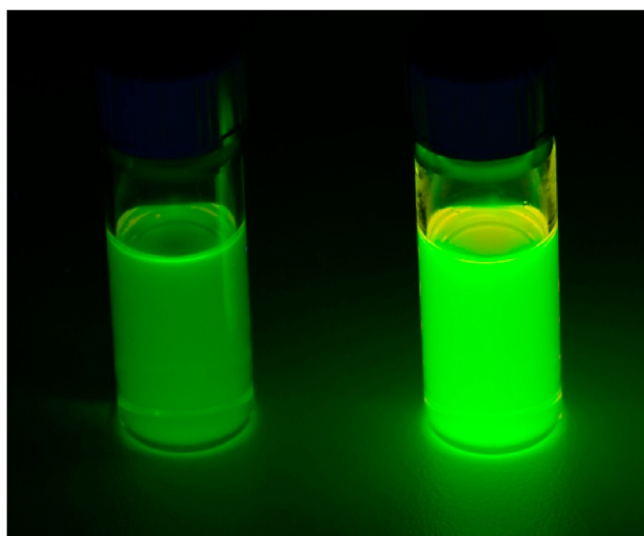

Figure 1. Photograph of two vials containing CdSe nanocrystals dispersed in hexanes under ultraviolet illumination. The nanocrystals in the left vial are undoped, while the particles in the right vial contain 2.7 Ag impurities per nanocrystal on average. The presence of the dopant leads to a roughly 10-fold enhancement in the fluorescence intensity. Adapted with permission from ref 22. Copyright 2012 American Chemical Society.

A second example of the influence of impurities on the physical properties of nanostructures is in electrical conduction. The incorporation of electronically active impurities can help engineer charge transport in devices that require nanometer-scale semiconductor channels.[23] For example, much effort has been placed on controlling the axial and radial dopant distributions in semiconductor nanowires.[24−27] As in bulk semiconductors, the presence of extra carriers provided by these dopants can help tailor charge transport.

Similarly, the incorporation of magnetic impurity atoms can be used to control the magnetic properties of semiconductor nanostructures.[28−33] Magnetic-impurity doping can lead to the creation of spintronic devices, such as spin filters and spin transistors.[34] For example, when the spin of electrons entering a quantum dot is aligned with the spin of its magnetic impurity, the quantum dot can act as a filter. Electrons with spins polarized in one direction are preferentially conducted, while electrons with opposing spins are blocked, thus enhancing or suppressing the spin-polarized current.[34]

Beyond obtaining new physical properties, impurities are also playing an increasingly important role in the synthesis of nanostructures. Namely, cation-exchange reactions have been exploited to convert nanostructures from one material to another.[35−37] For example, when CdSe nanocrystals are exposed to Ag cations in solution, the Ag^+ ions quickly displace all of the Cd^{2+} ions in the material, yielding Ag_2Se nanocrystals, as shown in Figure 2. In general, this route has been explored to obtain new structures that are difficult to synthesize directly, at least in the desired size or quality. In other words, if a well-developed material system can be used as a starting material and converted to another solid by simply exposing it to impurities, this provides an attractive approach to new materials.[38]

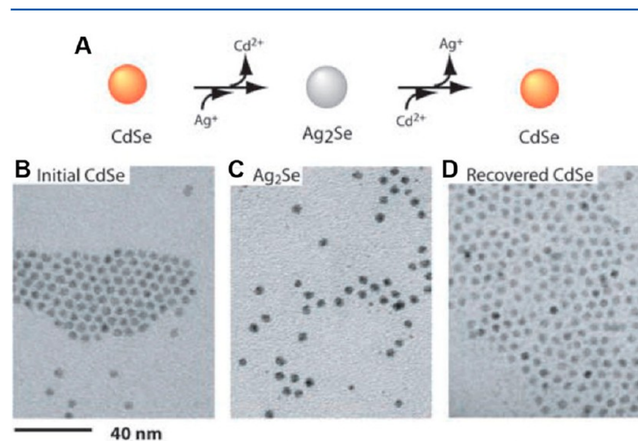

Figure 2. (A) Reaction scheme illustrating the cation-exchange reaction that transforms CdSe nanocrystals to Ag_2Se and partially back to CdSe. (B−D) TEM images of (B) the initial CdSe nanocrystals, (C) the resulting Ag_2Se nanocrystals after cation exchange, and (D) the nanocrystals recovered after partial transformation back to CdSe. Reprinted with permission from ref 36. Copyright 2004 American Association for the Advancement of Science.

Solid-state reactions involving impurities are also important for the formation of contacts in semiconductor nanoelectronic devices[39,40] and for electrochemical devices such as Li-ion batteries.[41−44] Traditionally, Li-ion batteries use graphite anodes, but semiconductor materials like Si and Ge have theoretical storage capacities an order of magnitude higher than graphite. When a battery anode is lithiated, Li impurities that enter the anode material are used to store electrochemical energy. However, the incorporation of large quantities of Li can cause an extremely large volume expansion, which can lead to cracking and deformation in bulk anode materials, thus

breaking electrical contact with the rest of the battery.[41] The mechanical deformation associated with the incorporation of Li impurities has led researchers to develop nanostructured Si and Ge anode materials that are capable of compensating for the very large volume expansions.[41−44]

However, in all of the examples mentioned above, we have an incomplete understanding of the underlying fundamental phenomena and mechanisms. Thus, it would be extremely helpful if we had knowledge of the location, number, and distribution of impurities in a specific nanostructure. This would aid studies trying to unravel the physical properties of doped nanostructures. It would also facilitate work trying to understand solid-state reactions, such as the cation-exchange process, which is heavily used but poorly understood. More broadly, fundamental knowledge about such reactions, including how impurities diffuse through the lattice, would aid the development of applications such as Li-ion batteries.

This review focuses on recent developments that try to address these issues. Namely, we discuss techniques that enable the direct imaging of impurity atoms in semiconductor nanostructures. After a brief overview of the challenges associated with impurities in nanostructures and their characterization, we review in situ transmission electron microscopy (TEM) experiments that allow solid-state reactions and impurity diffusion to be imaged in real time in the electron microscope. Then, we cover the use of atom probe tomography (APT) to construct three-dimensional atomic maps that depict the location and distribution of impurity atoms within a nanostructure. Finally, we review advanced electron microscopy techniques, such as electron energy loss spectroscopy (EELS) and annular dark-field scanning transmission electron microscopy (ADF-STEM), which allow individual atomic impurities in semiconductor nanostructures to be detected and imaged.

II. CHALLENGES IN DOPED NANOSTRUCTURES

Small nanostructures may contain only ~1000 atoms. As a result, a nanostructure that has a high dopant concentration from the bulk perspective may only contain a few impurity atoms. The properties of these structures can be seriously affected by statistical fluctuations in the number of impurities that are present.[45] Specifically, the probability $P(n)$ that a given nanostructure, within a sample with impurity mole fraction x, will contain n impurity atoms is given by the Poisson distribution, where N is the number of sites available for impurity incorporation:[46]

$$P(n) = \frac{(xN)^x e^{-xN}}{n!} \quad (1)$$

In particular, if a sample of quantum dots contains one impurity atom per particle on average, eq 1 indicates that roughly one-third of the particles have no impurities, one-third contain 1 impurity, and one-third contain more than one impurity. Clearly, nanostructures that contain zero, one, or two impurities may behave quite differently. However, if an experiment examines an ensemble of structures, only the average behavior will be measured. In order to elucidate the real effects of incorporating a specific number of impurity atoms into a nanostructure, methods of characterizing dopant atoms within an *individual* nanostructure would be extremely helpful.[17]

Fluctuations in the number of impurities in each nanostructure are also not the only complication. The location of the impurities can be an important factor. For example, in colloidal quantum dots, the properties of impurities can change if they are located in the center of the particle or near the surface or interface. This can influence the energy of the electronic states of the impurities.[47] Impurity location has also been used to tune the color of fluorescent impurities in semiconductor nanocrystals.[20] Likewise, when multiple impurity atoms are incorporated into a nanostructure, do the dopants exist in separate, individual locations, or do they form pairs and clusters? How does this affect the properties of the nanostructure? Methods to determine where impurities are located within an individual nanostructure would help us understand such effects.

Ideally, one would also determine the exact position of the impurities within the unit cell of the crystal lattice. In particular, for electronically active dopants, it matters whether the impurity atom is a substitutional or interstitial defect. For example, in Ag-doped CdSe nanocrystals, Ag is substitutional when it replaces Cd in the lattice. In this case, Ag, which has only one valence electron, replaces Cd, which has two. Ag consequently provides an extra hole and acts as a *p*-type dopant (known as an acceptor). Alternatively, Ag can also be interstitial when it squeezes between the Cd and Se atoms in the lattice. In this case, Ag can donate its one valence electron directly to the semiconductor and, hence, acts as an *n*-type dopant (known as a donor). Optical and electrical measurements performed on Ag-doped CdSe nanocrystals have shown nonmonotonic trends that suggest that Ag can act either as a substitutional or an interstitial defect, depending on the impurity concentration.[22] Simple methods that allow the position of the dopant within the nanostructure to be determined could provide clear evidence to resolve this and other related questions.

Spectroscopic techniques are available that can provide some information for certain classes of dopants. For example, the environment around impurities with unpaired spins (such as Mn) can be determined via electron paramagnetic resonance (EPR)[19,48−50] or magnetic circular dichroism (MCD) experiments.[19,28,32] Therefore, it is possible to resolve whether a Mn impurity has been incorporated into the lattice of a semiconductor nanocrystal or if the impurity is simply adsorbed on the nanocrystal surface. Unfortunately, these techniques have limited applicability. For impurity atoms without unpaired spins, they cannot provide such information. In these cases, if the impurity atom happens to have a nucleus suited to nuclear magnetic resonance (NMR) spectroscopy, it is possible that the local structure around the impurity atom can be determined with this technique.[51] Likewise, extended X-ray absorption fine structure (EXAFS) spectroscopy can provide information about the local environment around an impurity atom, for example, determining whether an impurity atom is in an interstitial or substitutional configuration.[22,52,53] However, while all of these techniques can clearly provide important information, some questions cannot be addressed. Namely, they cannot determine the specific location of the impurity atoms within the nanostructure (e.g., near the center or the surface of the structure). Moreover, they always provide information that is averaged over all of the impurities in the sample. Thus, information about fluctuations in the number of impurities per nanostructure and their position within the nanostructure or lattice is obscured.

III. IMPURITY DYNAMICS: DIFFUSION AND SOLID-STATE REACTIONS

A different set of challenges exists for studying the dynamics of impurity motion in semiconductor nanostructures. Figure 3 shows an early example where TEM was used to study the diffusion of Au impurities into InAs nanocrystals.[54] In these experiments, aliquots were collected at different time points and then imaged in the electron microscope, giving a general idea of how the diffusion of the Au impurities progressed. In Figure 4, Kelvin probe force microscopy (KPFM) was used to measure the surface potential of phosphorus-doped Si nanowires as a function of depth by successively etching and removing annular sections of the nanowire.[27] Impurity diffusion coefficients were then inferred by calculating impurity profiles for various assumed diffusion coefficients and then matching the calculated profiles to the experimentally measured surface potentials. While both of these experiments provide enormously valuable data, neither provides direct information regarding the dynamics of the impurity diffusion process.

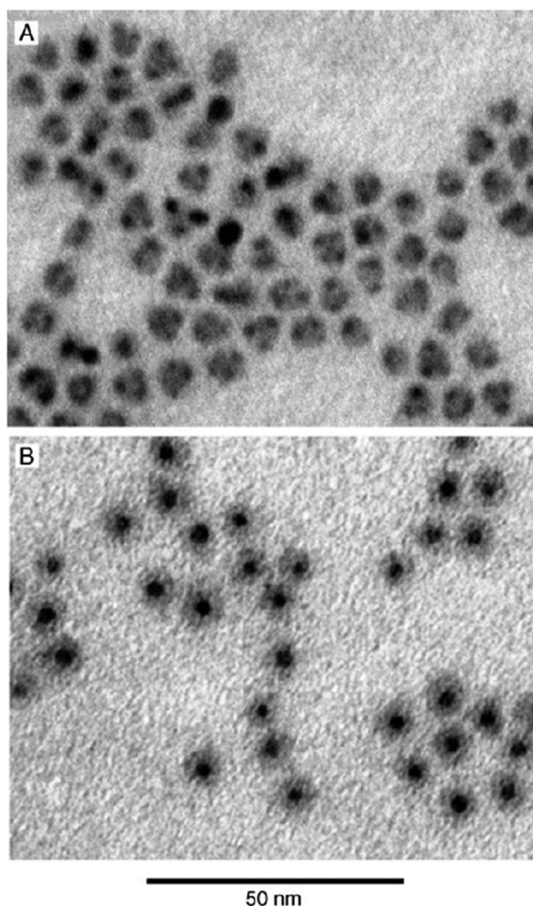

Figure 3. TEM images of InAs nanocrystals after Au impurities were allowed to diffuse into the nanostructures (A) for 2 h and (B) for 48 h. Reproduced with permission from ref 54. Copyright 2006 John Wiley & Sons.

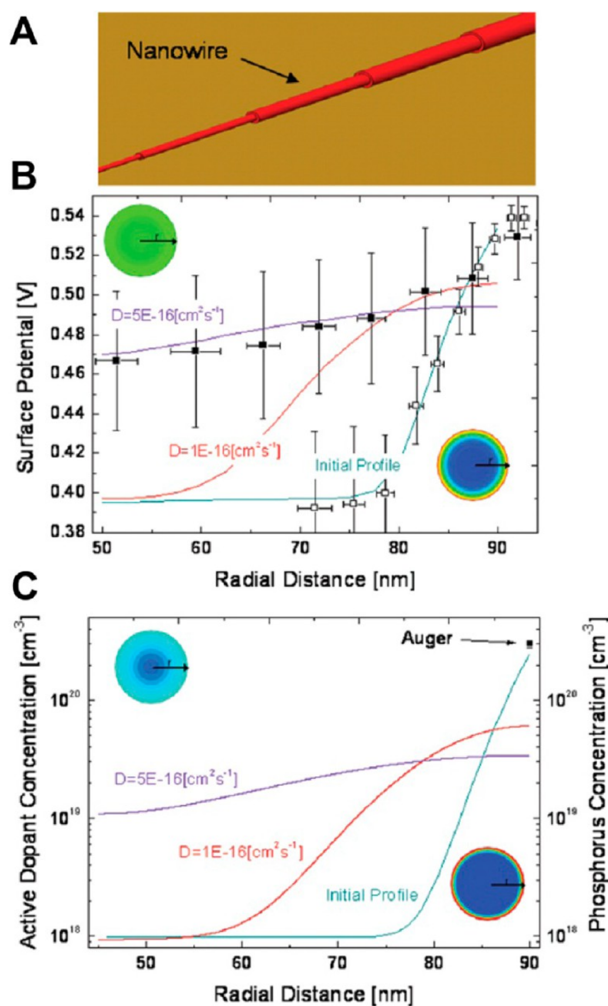

Figure 4. (A) Schematic illustration showing how radial composition profiles were collected by successively etching and removing annular sections of a Si nanowire. (B) Nanowire surface potential as a function of depth, as measured by Kelvin probe force microscopy (KPFM) after successive etching steps. Surface potentials were measured for as-made nanowires (open symbols) and for nanowires processed with a 1 h drive-in at 460 °C (closed symbols). (C) The calculated dopant distribution for various impurity diffusion coefficients. Reproduced with permission from ref 27. Copyright 2011 American Chemical Society.

Recent advances in in situ transmission electron microscopy (TEM), where experiments are carried out within the electron microscope, allow information on dynamic processes in individual nanostructures to be collected in real time.[9,13,14,55−87] In situ sample holders now enable heating to over 1000 °C inside the electron microscope, allowing researchers to directly study phenomena such as melting,[9,13,55,56] thermal expansion,[57] coalescence,[58] pressure-induced flow,[13,59,60] growth,[61−65] and phase nucleation and crystallization in nanostructures.[13,66−69] Figure 5 shows several examples of in situ TEM experiments where pressure-induced flow, nanocrystal coalescence, and nanowire growth were studied using a heating stage. In addition to heating, in situ TEM holders that enable mechanical and electromechanical testing have been developed,[70] holders with in situ optical probes are becoming available,[71] and sealed liquid cells allow the in situ investigation of liquid-phase systems within the electron microscope.[72−76]

In any in situ electron microscopy experiment, it is important to consider the effects of the electron beam on the sample.[65,88] Figure 6 shows the maximum transferrable energy for a variety of elements as a function of displacement threshold energy (i.e., beam energy), as well as the energy transfer necessary to displace or sputter atoms from a sample. If the maximum

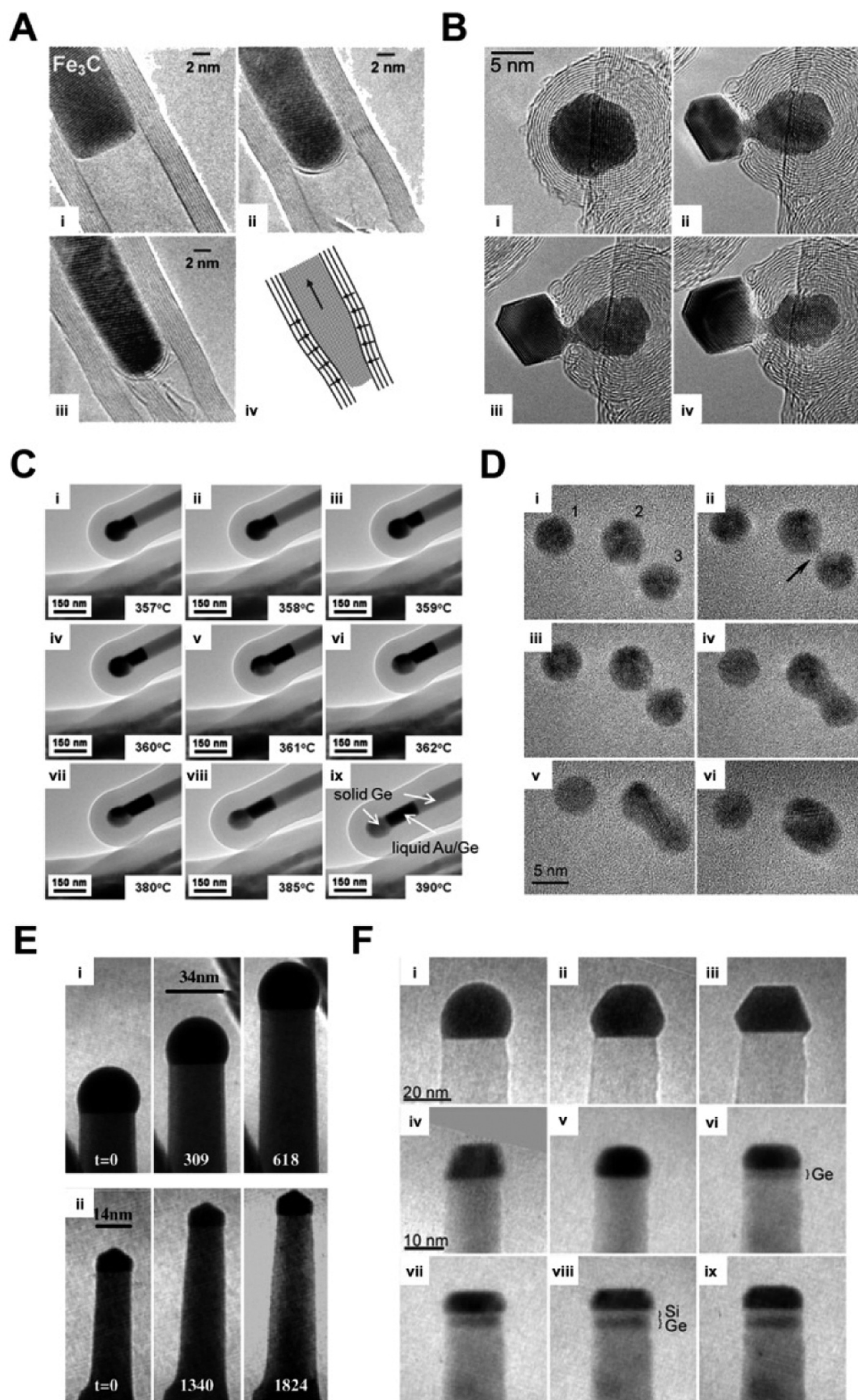

Figure 5. Examples of in situ TEM experiments. (A) Carbon-encapsulated Fe_3C being extruded under high pressure at 600 °C. Reprinted with permission from ref 59. Copyright 2006 American Association for the Advancement of Science. (B) Plastic deformation of carbon-encapsulated Au nanocrystals under high pressure at 300 °C. Reprinted with permission from ref 60. Copyright 2008 The American Physical Society. (C) Pressure-induced flow of liquid Au/Ge within a carbon-encapsulated Ge nanowire. Reprinted with permission from ref 13. Copyright 2009 American Association for the Advancement of Science. (D) Coalescence of Au nanocrystals at 400 °C. Reproduced with permission from ref 58. Copyright 2005 American Chemical Society. (E) Ge nanowire growth from (i) a liquid AuGe droplet and (ii) from a solid Au particle inside the electron microscope. Reprinted with permission from ref 61 and ref 65. Copyright 2007 American Association for the Advancement of Science and 2010 IOP Publishing. (F) Formation of axial Si−Ge−Si heterojunctions within a growing Si nanowire. Reprinted with permission from ref 64. Copyright 2009 American Association for the Advancement of Science.

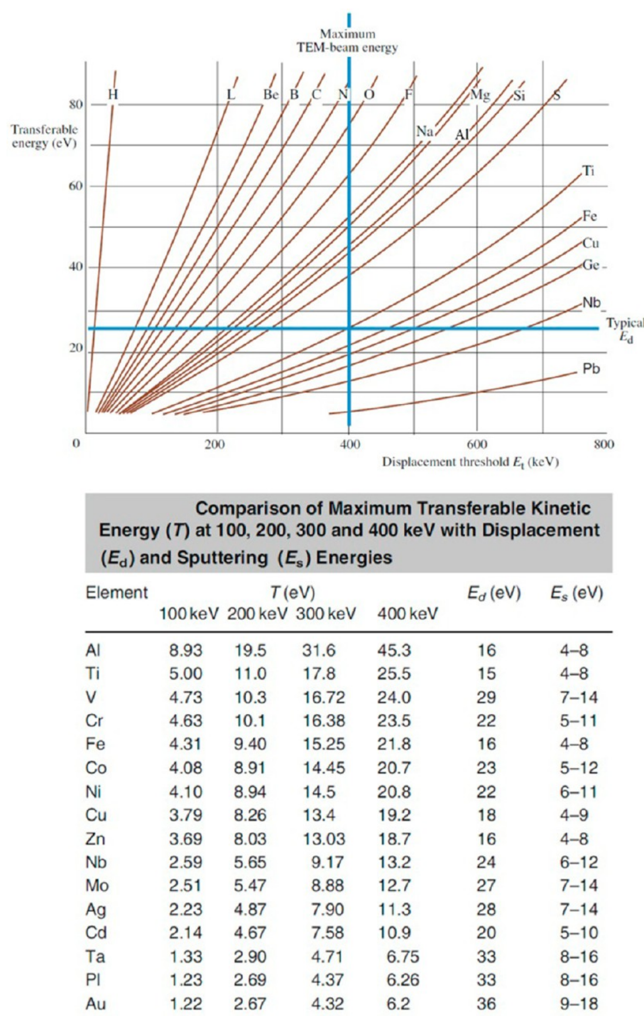

Comparison of Maximum Transferable Kinetic Energy (T) at 100, 200, 300 and 400 keV with Displacement (E_d) and Sputtering (E_s) Energies

Element	T (eV) 100 keV	200 keV	300 keV	400 keV	E_d (eV)	E_s (eV)
Al	8.93	19.5	31.6	45.3	16	4–8
Ti	5.00	11.0	17.8	25.5	15	4–8
V	4.73	10.3	16.72	24.0	29	7–14
Cr	4.63	10.1	16.38	23.5	22	5–11
Fe	4.31	9.40	15.25	21.8	16	4–8
Co	4.08	8.91	14.45	20.7	23	5–12
Ni	4.10	8.94	14.5	20.8	22	6–11
Cu	3.79	8.26	13.4	19.2	18	4–9
Zn	3.69	8.03	13.03	18.7	16	4–8
Nb	2.59	5.65	9.17	13.2	24	6–12
Mo	2.51	5.47	8.88	12.7	27	7–14
Ag	2.23	4.87	7.90	11.3	28	7–14
Cd	2.14	4.67	7.58	10.9	20	5–10
Ta	1.33	2.90	4.71	6.75	33	8–16
Pl	1.23	2.69	4.37	6.26	33	8–16
Au	1.22	2.67	4.32	6.2	36	9–18

Figure 6. Beam damage thresholds for a variety of elements. The curves indicate the maximum amount of energy that can be transferred to an atom of a given element for a given displacement threshold energy (i.e., beam energy). The table lists the energy transfer required to either displace E_d or sputter E_s an atom from the sample. If the maximum transferrable energy for a given accelerating voltage exceeds the displacement energy for an element, beam damage is likely to occur. Reproduced from ref 88 with kind permission from Springer Science and Business Media. Copyright 2009 Springer Science.

transferrable energy for a given accelerating voltage exceeds the displacement energy for an element, beam damage is likely to occur. For example, a sample of Ge is unlikely to experience knock-on damage when imaged in an electron microscope operated at 200 kV since the maximum transferrable energy to Ge at that accelerating voltage is around 7 eV and the displacement energy for Ge is 14.5 eV.[89] To exceed the Ge displacement energy and knock out Ge atoms, an accelerating voltage of 360 kV would be required.[14] However, a sample of Si imaged under the same conditions at 200 kV is very likely to experience significant beam damage. From Figure 6, the maximum transferrable energy to Si at an accelerating voltage of 200 kV is around 20 eV, and the displacement energy for Si is 12.9 eV.[89] Indeed, an accelerating voltage of only 145 kV is sufficient to knock out Si atoms.[14] Therefore, Si should be imaged at an accelerating voltage of less than 145 kV in order to ensure that beam damage does not affect the sample.

In addition to beam-induced displacement of atoms via sputtering and knock-on damage, electron-beam-induced chemical reactions and electron-beam heating may also occur.[65] At elevated temperatures, heating by the electron beam is often negligible since phonons generated by interaction with the electron beam are likely to increase the temperature of the sample by only a few degrees.[65] Heating effects are also mitigated when the sample has good thermal conductivity. However, at lower temperatures, the rise may be significant, and it is necessary to account for the effect of electron-beam heating. A high-intensity electron beam can also break bonds and cause chemical reactions to occur.[65] In some cases, electron-beam-induced deposition (EBID) is used as a tool to fabricate unique structures inside the electron microscope,[13,77] although more often than not, it is an unwanted side-effect. Both electron-beam heating and beam-induced deposition are intensified by focusing the electron beam on the sample. In any in situ TEM experiment, adjusting imaging conditions to minimize the beam energy and dose applied to the sample is the best approach to mitigate the effects of atomic displacement, electron-beam heating, and beam-induced deposition.

Recently, researchers have begun to use in situ electron microscopy as a tool to study impurity diffusion in thin slabs of bulk material, as well as in semiconductor nanostructures.[13,14,78] This approach has advantages over ex situ approaches since the diffusion process can be observed directly. Figure 7 shows an in situ TEM experiment investigating diffusion of Si impurities along dislocation cores bridging Si precipitates in a thin slab of Al at 350 °C.[78] In this study, dislocations that bridge Si precipitates in an Al sample were observed to act as conduits for Si diffusion, facilitating Ostwald ripening between precipitates of different sizes.[78] Prior to this study, this diffusion process, known as pipe diffusion, had only been measured indirectly, although it has been used as an explanation for a variety of different phenomena.[78] Here, the authors were able to directly observe the phenomena and were able to determine diffusion coefficients for Si pipe diffusion along an Al dislocation core, finding that dislocations accelerate impurity diffusion by 3 orders of magnitude relative to bulk diffusion.[78] The measured diffusion coefficients for pipe diffusion of Si in Al were found to be similar to diffusion coefficients for Al pipe self-diffusion.[90,91]

Figure 8 presents a study where in situ TEM was used to investigate the diffusion of Au impurities in single-crystalline Ge nanowires.[13] A nanoscale reservoir of Au was formed by melting the Au catalyst on the end of a carbon-encapsulated Ge nanowire, forming a liquid Au/Ge melt. At high temperature, where the solid solubility of Au in Ge begins to increase, Au impurities leave the reservoir and begin to diffuse through the Ge nanowire.[13] Interestingly, the measured diffusion coefficients were orders of magnitude lower than the diffusion coefficients for Au diffusion in bulk Ge. Au can occupy both substitutional and interstitial sites in Ge, and in general the number of substitutional Au impurities at a given temperature is much greater than the number of interstitial Au impurities. However, interstitial Au diffuses many orders of magnitude faster than substitutional Au, which diffuses via a vacancy-mediated mechanism.[13] In this particular case, where a nanoscale Au reservoir was used, not enough Au atoms were present in the system to generate a population of interstitial Au. Thus, only the vacancy-mediated diffusion of substitutional Au impurities was observed.[13] Clearly, boundary conditions can have a dramatic effect on impurity diffusion in semiconductor

dx.doi.org/10.1021/cm400004x | Chem. Mater. 2013, 25, 1332−1350

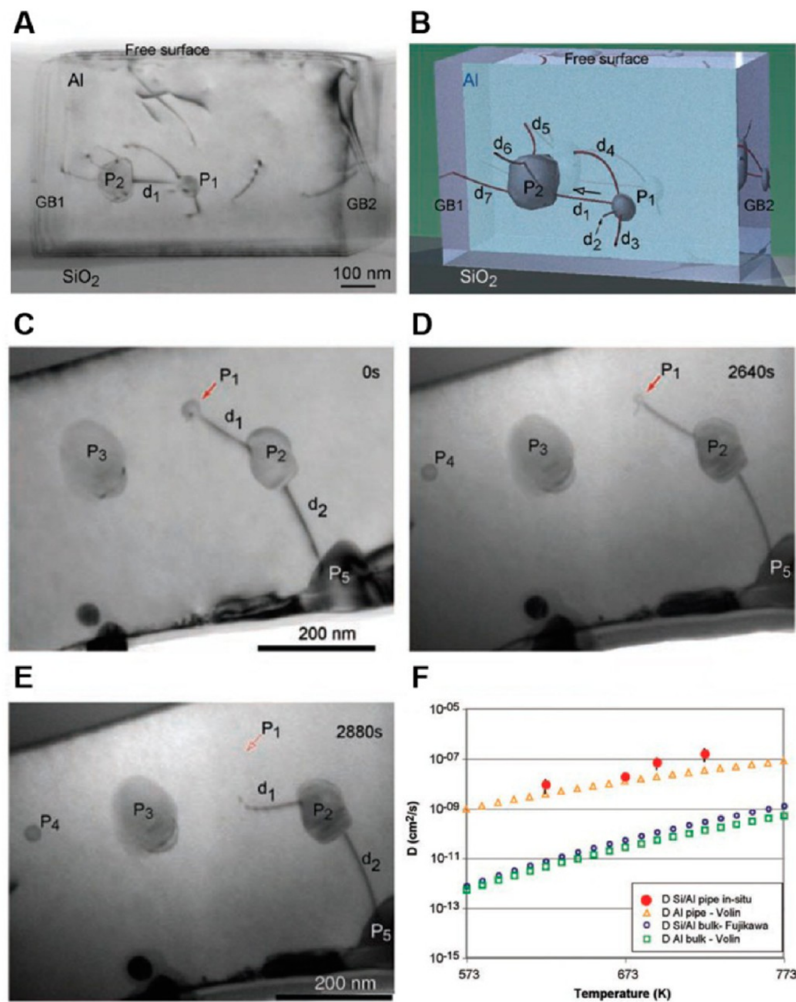

Figure 7. (A) TEM image of Si precipitates and dislocations in an Al slab. (B) Schematic of the Si precipitates (P_i) and dislocation segments (d_i) in the sample shown in (A). (C–E) In situ TEM experiment showing the dissolution of Si precipitate P_1 at 350 °C as Si diffuses along dislocation segment d_1 from P_1 to P_2. In (E) dislocation segment d_1 is released once P_1 has completely dissolved. (F) Measured diffusion coefficients for Si pipe diffusion in Al (filled red circles) as compared to Al pipe self-diffusion (open orange triangles),[90] lattice self-diffusion of Al (open green squares),[90] and lattice diffusion of Si in Al (open blue circles).[91] See the Supporting Online Material in ref 78 for a video showing the dissolution of a Si precipitate via pipe diffusion. Reprinted with permission from ref 78. Copyright 2008 American Association for the Advancement of Science.

nanostructures. As seen in Figure 8, the measured diffusion coefficients are similar to Ge self-diffusion, which is also mediated by vacancies.

In situ TEM has also been used to investigate impurity diffusion in Si nanowires.[14] Figure 9A–B demonstrates how atomic-number (Z) contrast can be used to track impurity diffusion, and Figure 9C shows images of Au diffusion in a Si nanowire at 800 °C. In this experiment, a TEM grid made of Au foil was used as the diffusion source. It was observed that Au diffused extremely quickly, with the diffusion front advancing at velocities greater than 10 000 nm/s close to the metal source.[14] In this case, the metal grid acts as an effectively infinite diffusion source, supplying enough Au atoms to the system for interstitial Au diffusion to play a significant role. The observed diffusion coefficients in this situation were one to two orders of magnitude greater than Au diffusion in bulk Si (Figure 9D), suggesting that nanowires may support a higher concentration of interstitial Au than bulk Si.[14] Again, boundary conditions play a very important role in impurity diffusion on the nanoscale.

Beyond diffusion, in situ TEM can be exploited to understand phase transitions and solid-state reactions in nanostructures.[13,14,79−87] For example, silicide formation can be very important for making low resistance electrical contacts in transistors.[14,39,40,79−81] Several recent reports have studied silicide formation in Si nanowires.[14,40,79−81] Figure 9E–F shows the transformation of Si nanowires to $NiSi_2$ and Cu_3Si.[14] During this process, impurity atoms diffuse through the silicide phase to the silicide/Si interface, where they react to form additional silicide. As such, silicide formation can be limited by either the diffusion of impurity atoms through the silicide layer or by the reaction rate at the interface. In situ TEM studies have demonstrated that Cu_3Si formation in Si nanowires is diffusion limited[14] and that $NiSi_2$ and Ni_2Si formation are also diffusion limited,[14,79] as are most bulk silicides. Interestingly, in situ TEM experiments also indicate that $NiSi_2$ transitions from an initial reaction-rate-limited growth stage to a diffusion-limited growth stage at later times[79]—a difficult observation to make without the aid of in situ experiments.

The incorporation of metal impurities into the Si lattice during silicide formation can also lead to very large volume

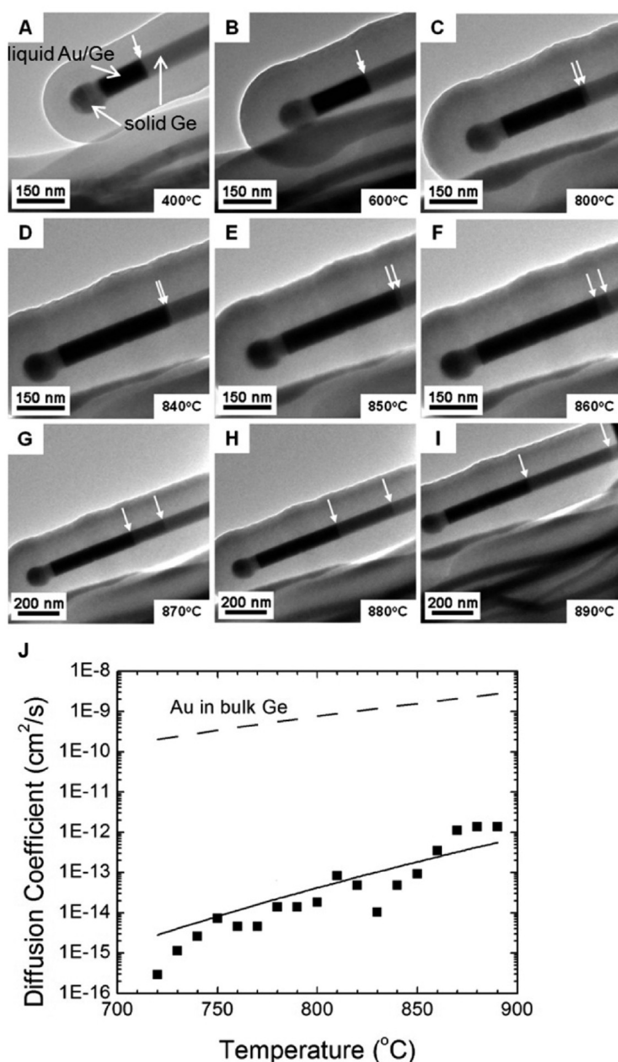

Figure 8. (A–I) Images from an in situ TEM experiment investigating the diffusion of Au atoms in a carbon-encapsulated Ge nanowire. The Au source is a nanoscale Au/Ge reservoir (black) formed by melting the Au catalyst on the end of the nanowire. At high temperatures, where the solid solubility of Au in Ge begins to increase, Au impurities begin to diffuse through the Ge nanowire (region bracketed by the white arrows). (J) Measured diffusion coefficients for the diffusion of Au impurities from a nanoscale reservoir through a Ge nanowire (black squares). The dashed black line corresponds to the diffusion of Au impurities in bulk Ge, and the solid black line corresponds to Ge self-diffusion. See the Supporting Online Material in ref 13 for a video showing the diffusion of Au in a Ge nanowire. Reprinted with permission from ref 13. Copyright 2009 American Association for the Advancement of Science.

expansions. Nickel silicides form a variety of phases, including Ni_3Si, $Ni_{31}Si_{12}$, Ni_2Si, Ni_3Si_2, NiSi, and $NiSi_2$, with volume changes ranging from 1.3 to 115%.[14,40] It has been shown via in situ TEM that restricting the volume of Si nanowires with either an oxide or carbon shell can lead to the selective formation of silicide phases with minimal volume expansion.[14,80] The transformation of Si into Cu_3Si leads to a volume expansion of nearly 150%, as can be seen in Figure 9F. However, encapsulation of a Si nanowire in a carbon shell prior to silicide formation leads to the formation of a copper silicide phase with little volume expansion (most likely $CuSi_2$) and Cu diffusion rates nearly 2 orders of magnitude slower than in Cu_3Si (Figure 9D).[14]

For battery applications, the fact that materials such as Si and Ge can incorporate extremely large quantities of Li is both beneficial and problematic. The more Li that a battery can incorporate, the higher its energy storage capacity. At the same time, the incorporation of Li impurities leads to extremely large volume expansions (400% for Si), which can lead to pulverization and separation of the electrode. Nanostructured electrodes have been shown to accommodate the volume expansion associated with lithiation, resulting in electrode materials more resilient to repeated cycling.

In situ TEM has proven to be an invaluable technique for studying lithiation and delithiation in a variety of anode materials.[82−85] Figure 10 shows an investigation of the electrochemical lithiation of a SnO_2 nanowire anode.[82] In this experiment, SnO_2 nanowires mounted on a Au electrode were brought into contact with an ionic-liquid electrolyte on the end of a $LiCoO_2$ counter electrode inside the electron microscope (Figure 10A).[82] After the ionic-liquid electrolyte wicked up the surface of the nanowire, a −3.5 V potential was applied, initiating electrochemical lithiation of the SnO_2 nanowire anode.[82] It should be noted that bulk SnO_2 is a brittle material, but in this case, the SnO_2 nanowire was able to flex and plastically deform. As the Li impurities moved through the nanostructure, it bent and twisted, elongating 60% and expanding 45% in the lateral direction, accommodating a total volume expansion of 240%.[82] The solid-state reaction proceeds via an advancing dislocation cloud at the reaction interface, transforming the single-crystalline SnO_2 nanowire to an amorphous, lithiated nanostructure as the reaction front moves down the nanowire (Figure 10I−N). This type of in situ analysis provides valuable mechanistic information about how nanowires accommodate strain during the incorporation of Li impurities.

Figure 11 shows an analogous study conducted on a Si nanowire anode.[83] In these experiments, it was found that doping the nanowires with phosphorus and adding a carbon coating increased the charging rate by an order of magnitude.[83] As in the case of the SnO_2 nanowire above, the high charging rate caused the lithiating Si nanowire to spiral and twist as Li impurities were incorporated, resulting in a volume expansion of roughly 300%. The charging rates in this investigation are the highest reported for the lithiation of Si electrodes, providing important information for the design of advanced batteries. For more information on in situ TEM investigations of electrochemical lithiation and delithiation of C, Si, Ge, and metal oxide nanostructures, the reader is directed to the review by Liu et al.[85]

IV. IMPURITY CONCENTRATION PROFILES

In addition to TEM, another powerful tool for determining the location of impurity atoms within a material is atom probe tomography (APT). The origins of the atom probe are based on Erwin Müller's work in field ionization and field ion microscopy (FIM) in the 1930s and 1940s.[92] By coupling the field ion microscope to a time-of-flight (TOF) mass spectrometer, the atom probe was born, with the first paper on the subject published by Müller et al. in 1968.[93]

The design of the atom probe has evolved significantly over the years, but Figure 12 illustrates the fundamental operating principle of the microscope.[94] A sharp needle-shaped specimen is attached to an electrode, and a very high bias (on the order of

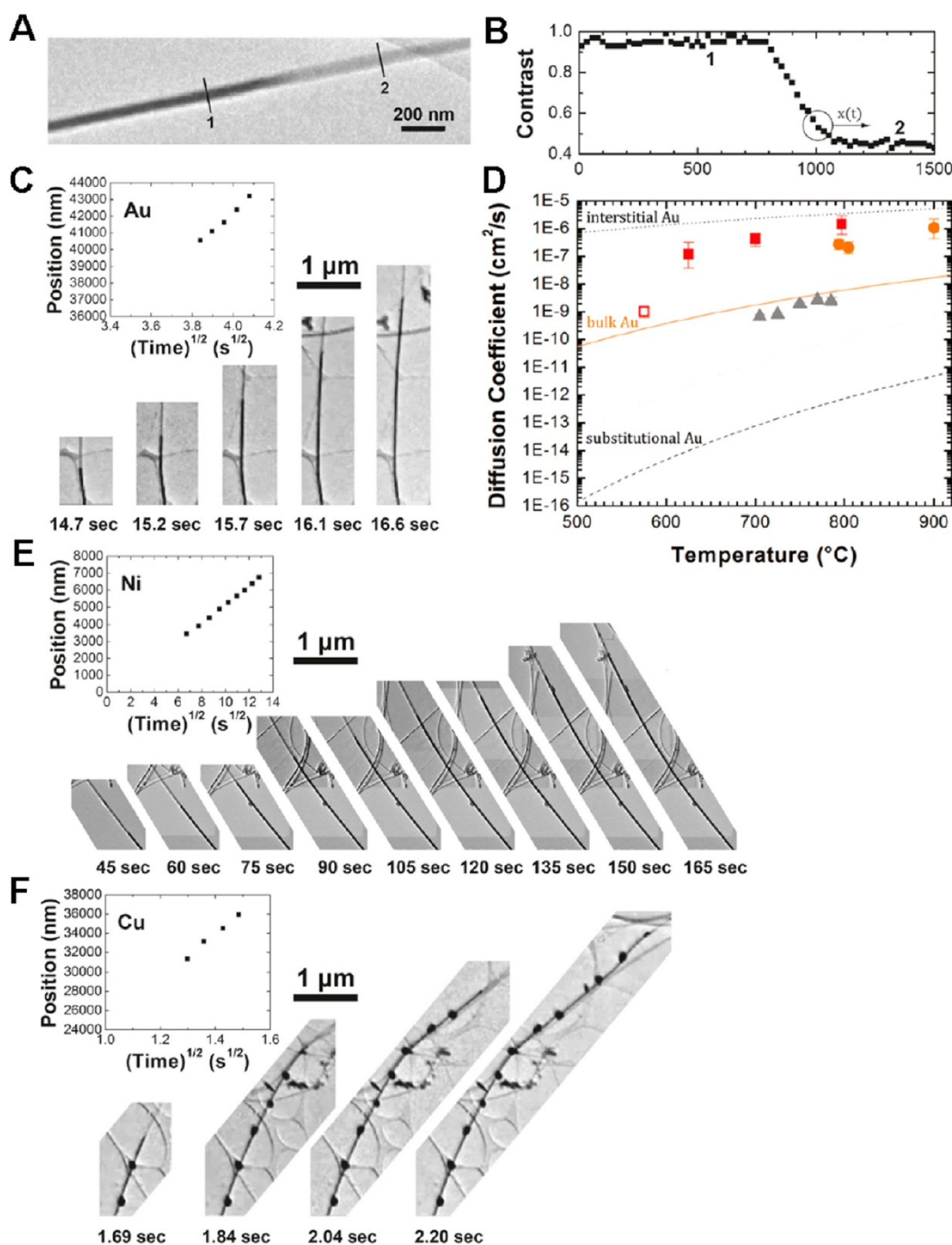

Figure 9. (A) TEM image of impurities diffusing in a Si nanowire. (B) Axial contrast profile taken down the centerline of the nanowire shown in (A). (C) TEM images of Au diffusing in a Si nanowire at 800 °C. (D) Measured diffusion coefficients for Au (gold circles), Ni (gray triangles), and Cu (red squares) in Si nanowires. In all cases, metal foil TEM grids were used as the diffusion source. The open square corresponds to Cu diffusion in a carbon-encapsulated Si nanowire that was exposed to 200 keV electron radiation for 1 h. The bulk effective diffusion coefficient for Au in crystalline Si (solid gold line) is plotted for reference, along with the diffusion coefficients for interstitial (dotted line) and substitutional Au (dashed line). (E) TEM images of an advancing Ni front in a Si nanowire at 700 °C and (F) Cu moving through a Si nanowire at 800 °C. See the Supporting Information in ref 14 for a video showing the diffusion of Au in a Si nanowire and videos showing the transformation of Si nanowires to nickel and copper silicide. Reproduced with permission from ref 14. Copyright 2011 American Chemical Society.

5−20 kV) is applied between the sample and a counter electrode. This results in a very large electric field (∼10−50 V/nm) at the apex of the needle. The bias is held just below the field evaporation threshold of the sample material, and then a short subnanosecond voltage pulse (1−3 kV) or laser pulse is applied to the sample tip, causing an ion to field evaporate from the surface.[95] The energy of the pulse is generally very small, such that atoms are removed essentially one at a time. By measuring the time-of-flight between the evaporation pulse and the detection event on a two-dimensional, position-sensitive detector, the mass-to-charge ratio of the field-evaporated ion can be determined.[95] By recording the position of the ion on the imaging detector, the origin of the field-evaporated ion can be traced back along the field lines, thus allowing the three-dimensional reconstruction of the sample ion by ion, with the identity of each ion determined by its mass-to-charge ratio.[95]

One recent advance in APT was the development of the local electrode atom probe (LEAP), which uses a local electrode with a very small aperture that is positioned only micrometers from the sample tip (Figure 12B).[94] This configuration allows very high data collection rates (>10000 atoms/s) and a much larger field of view (>100 nm diameter), enabling the full three-

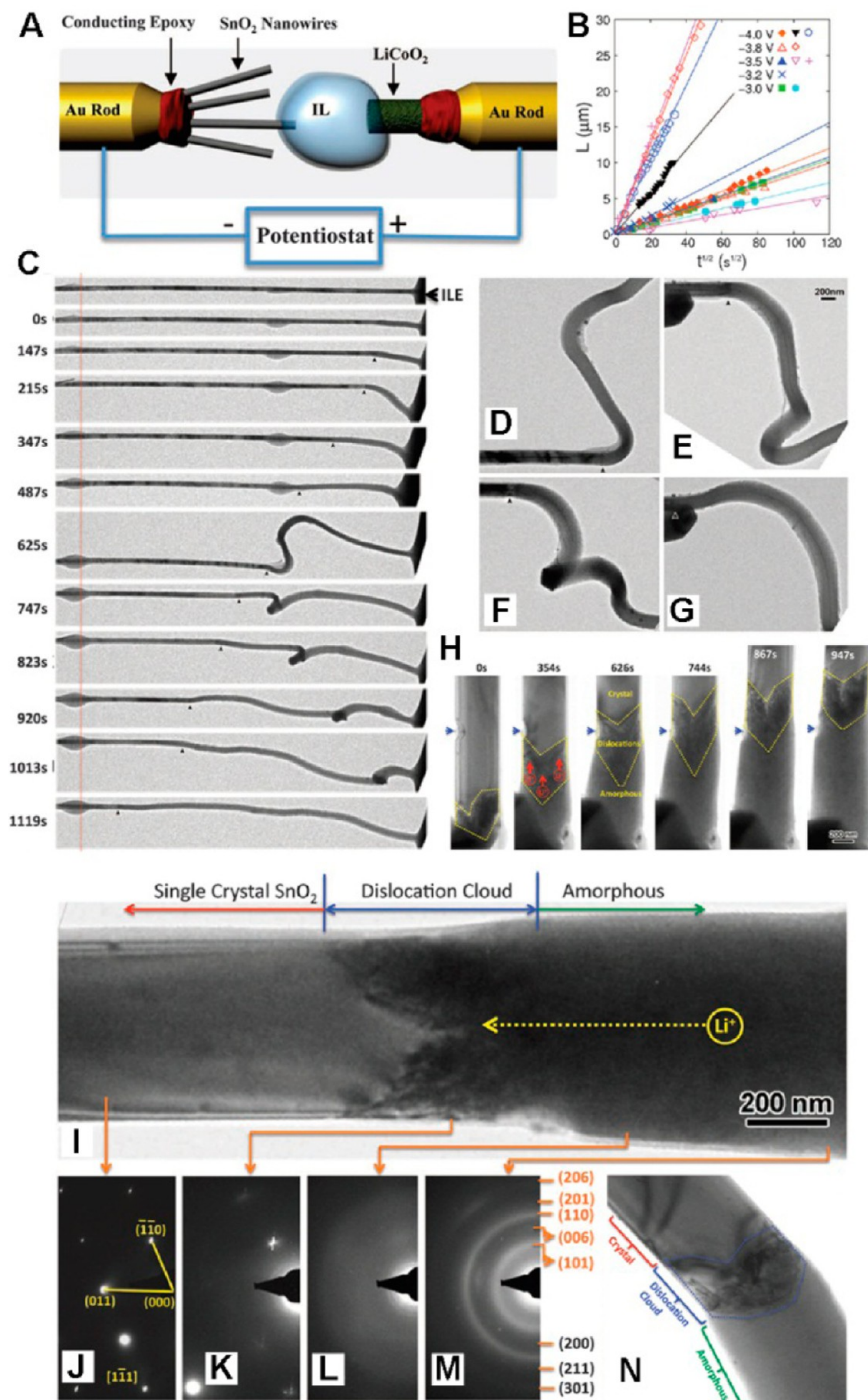

Figure 10. In situ electrochemical lithiation of a SnO_2 nanowire anode during charging at −3.5 V versus a $LiCoO_2$ cathode. (A) Schematic diagram of the electrochemical cell used in the lithiation experiment. (B) Position of the reaction front as a function of the square root of time, illustrating that the lithiation process is diffusion limited. (C) Time progression of the morphological changes that occur during lithiation. (D−G) TEM images showing deformed sections of the lithiated nanowire. (H) Time progression showing the migration of the dislocation cloud at the reaction interface. (I) TEM image of the three distinct areas around the reaction zone and (J−M) electron diffraction patterns of the regions indicated in I. The diffraction rings in M are due to small Sn and Li_xSn crystallites that form within the amorphous section of the lithiated nanowire. (N) TEM image showing the crystalline and amorphous regions of the nanowire surrounding the dislocation cloud. See the Supporting Online Material in ref 82 for videos showing the electrochemical lithiation of SnO_2 nanowires. Reprinted with permission from ref 82. Copyright 2010 American Association for the Advancement of Science.

dimensional reconstruction of 10^6 nm^3 volumes containing hundreds of millions of atoms.[96] The atom probe can deliver a spatial resolution of less than 0.3 nm, although the achievable resolution is limited by several factors, including the shape, orientation, and material properties of the specimen.[97,98] The spatial resolution is also anisotropic, with an axial resolution of less than 0.1 nm and a lateral resolution of less than 1 nm.[98] APT is also able to detect impurities at an analytical sensitivity of better than 10^{18} cm^{-3}.[97] However, it is important to note that a large number of atoms must be collected to achieve such

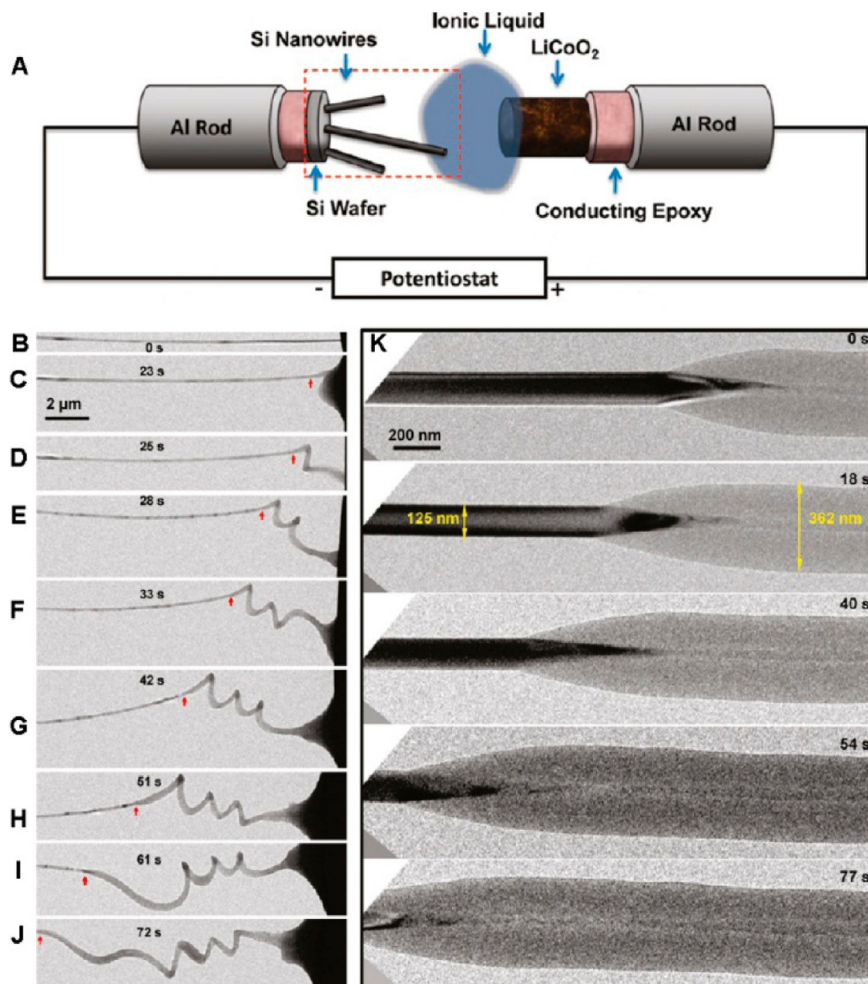

Figure 11. In situ electrochemical lithiation of a carbon-coated, phosphorus-doped Si nanowire anode charging at −4 V versus a $LiCoO_2$ cathode. (A) Schematic diagram of the electrochemical cell. (B−J) Time progression of the morphological changes that occur during lithiation of the Si nanowire. (K) Progression showing how the nanowire accommodates the enormous volume expansion associated with Si lithiation. See the Supporting Information in ref 83 for videos showing the electrochemical lithiation of Si nanowires. Reproduced with permission from ref 83. Copyright 2011 American Chemical Society.

high levels of sensitivity since only a fraction of the atoms in the sample volume are actually detected. The detection efficiency is a maximum of 60% for the position-sensitive crossed delay line detectors currently used in most atom probe instruments.[97] Improvements in detector technology would help extend the analytical sensitivity of APT to much smaller sample volumes.

In order to achieve electric fields sufficient for field evaporation, the sample tip must be very sharp, having a radius of curvature on the order of 10−100 nm.[99] These geometric constraints place a fundamental limit on the types of samples that can be analyzed via APT. Figure 13 illustrates the fabrication of a sharp tip from a sample by annular milling with a focused ion beam (FIB).[100] Figure 14 shows an example of an APT reconstruction of a sample tip fashioned from a B-doped Si calibration sample, along with a comparison between the composition profile determined from LEAP analysis and from a secondary ion mass spectroscopy (SIMS) analysis performed by the U.S. National Institute of Standards and Technology (NIST).[101] The composition profile determined by APT is virtually identical to the SIMS calibration performed by NIST. Clearly, APT provides an attractive alternative strategy for accurately determining the distribution of impurity atoms within nanoscale semiconductors.

Figure 15 shows two more examples of atomic reconstructions generated by APT with a LEAP instrument.[101] Figure 15A shows the abrupt interface between layers in a Si/SiGe stack, and Figure 15B−D shows an APT reconstruction of a multilayer photovoltaic device consisting of GaAs, InGaP, and In-doped GaAs layers, along with the corresponding concentration profiles.[101]

In addition to samples fashioned using a FIB, semiconductor nanowires are ideal subjects for APT analysis due to their inherent needle-like geometry.[102−106] Figure 16 shows an atomic reconstruction of an InAs nanowire and the Au catalyst particle on its tip.[102] Au impurities are clearly visible throughout the nanowire, likely distributed during the nanowire growth process. Similar analyses have been performed on doped Si and Ge nanowires to determine the distribution of B and P impurities within the nanostructure.[103−105] Figure 17 shows the distribution of P atoms in a Ge nanowire, revealing a highly doped shell region in the outer 12 nm of the nanowire.[104] Recent APT analysis of phosphorus-doped Ge and boron-doped Si nanowires indicates that impurity incorporation may be facet-dependent, with impurities being selectively incorporated along corner facets during nanowire growth.[106]

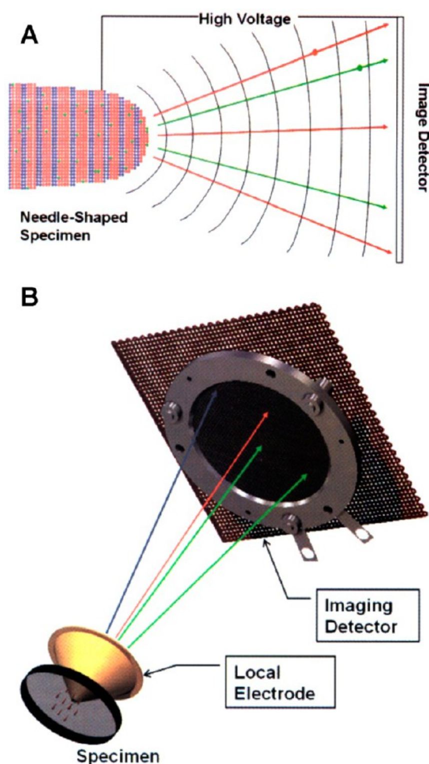

Figure 12. Schematic diagram illustrating (A) the basis of atom probe operation and (B) the general design of a local electrode atom probe (LEAP) microscope. Reprinted with permission from ref 94. Copyright 2003 Cambridge University Press.

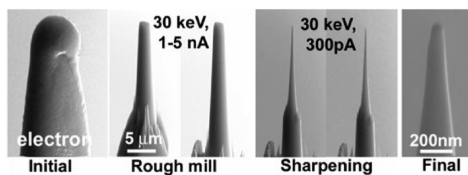

Figure 13. SEM images showing the final sample preparation steps for APT, where a micrometer-scale sample (left) is gradually sharpened via annular milling with a focused ion beam (FIB). As the needle is slowly sharpened with the Ga beam, the size of the annular milling mask and the ion current are progressively reduced. The final needle, with sub-100 nm radius of curvature, is shown on the right. Reprinted with permission from ref 100. Copyright 2007 Cambridge University Press.

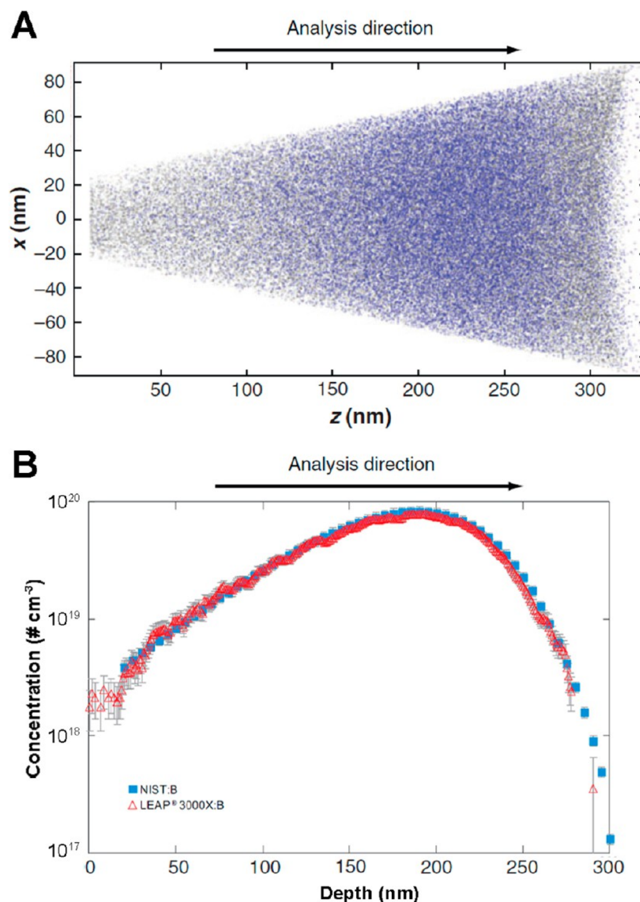

Figure 14. (A) Two-dimensional projection of a three-dimensional atomic reconstruction of a B-doped Si sample generated by APT with a LEAP instrument (included with kind permission of Sean Corcoran). Blue dots correspond to ^{10}Bi atoms and gray dots correspond to Si atoms. (B) ^{10}B concentration profile determined via APT analysis (open red triangles) and via SIMS analysis by NIST (solid blue squares). Reproduced with permission from ref 101. Copyright 2007 Annual Reviews.

V. IMAGING INDIVIDUAL IMPURITY ATOMS

New methods for imaging individual impurities have also recently been developed due to new advances in scanning transmission electron microscopes (STEMs). Indeed, since the introduction of the first modern STEM,[107,108] the field of transmission electron microscopy has changed dramatically. Three critical components of the STEM—a high-brightness field-emission electron source, the ability to scan with a focused electron probe, and the annular-dark-field (ADF) detector—and the later addition of the electron energy-loss spectrometer, have made STEM a truly analytical scientific instrument, capable of very high precision measurements. The preference of the STEM over conventional TEM is governed, first, by the ability to record images of specimens by collecting elastically scattered electrons using a high-angle ADF detector. This allows the visualization of specimens with atomic resolution with a simple interpretation. Namely, heavier atoms lead to stronger electron scattering and, as a result, a brighter signal.[109,110] A second critical feature of the STEM is its ability to position a fine probe over any location in the specimen and measure the electron energy-loss spectrum (EELS) from that particular point. Alternatively, if linear averaging is required, spectra can be obtained from a single line by scanning the fine probe between two user-defined points. Additionally, since EELS and ADF imaging can be performed in parallel, spectroscopy with atomic-level precision is possible. Advances in aberration correction of magnetic electron optical lenses have made it possible to reduce the probe size down to the sub-Å level[111] and, as a result, have turned STEM into an analytical characterization tool with <1 Å lateral resolution.

When core-level electronic transitions are probed with EELS, it is possible to carry out an analysis of the local chemistry and electronic structure of a sample. Fermi's golden rule, which describes the physics of EELS transitions in a simple dipole approximation, shows the element- and site-specific nature of these localized core-level transitions.[112] This elemental and site-specific sensitivity has been illustrated by recording atomic-resolution spectroscopic images of $Bi_{0.5}Sr_{0.5}MnO_3$,[113] $La_{1.2}Sr_{1.8}Mn_2O_7$,[114] and $SrTiO_3$ crystals.[115]

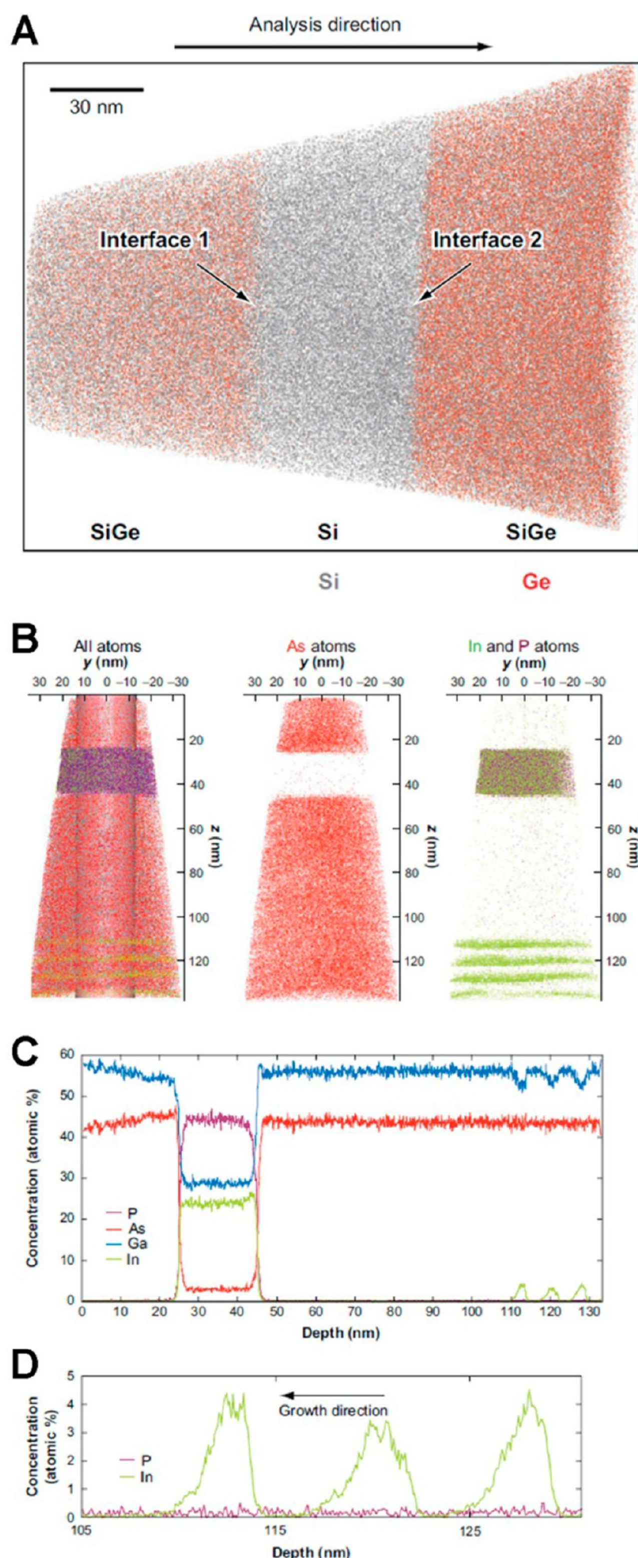

Figure 15. (A) APT reconstruction of a Si/SiGe multilayer stack. Si atoms are shown in gray, and Ge atoms are shown in red. (B) APT reconstruction of a multilayer photovoltaic device consisting of GaAs, InGaP, and In-doped GaAs layers. As atoms are shown in red, P atoms in violet, In atoms in green, and Ga atoms in gray. (C–D) Concentration profiles determined from the APT analysis. Reproduced with permission from ref 101. Copyright 2007 Annual Reviews.

While both conventional TEMs and STEMs are capable of imaging individual atoms,[108,116] detecting an individual impurity atom inside a crystal is easier using ADF-STEM. Here, as discussed before, the relatively simple relationship between ADF intensity and the atomic number of the scattering atoms enables direct visualization of lattice abnormalities in high-resolution images of crystalline specimens, including detection of single dopant atoms. However, some challenges in experimental identification of individual impurity atoms inside crystals using ADF-STEM images are still present. Among these challenges, the signal collected from impurity atoms must be sufficiently above experimental noise, dopant atoms must be carefully differentiated from atoms accidentally deposited on the surface of the sample, and electron-beam-induced specimen damage must be kept below a level that will limit analysis. Imaging impurity atoms in crystalline specimens is further complicated due to channeling of the incident electron beam along atomic columns,[117−120] which also places a depth dependence on impurity detection.

Despite such challenges, several groups have successfully imaged impurity atoms inside a host crystal using ADF-STEM, as demonstrated in Figure 18. For example, Voyles et al.[121] observed Sb atoms in Si (Figure 18A); Shibata et al.[122] imaged Y atoms in Al_2O_3 (Figure 18D); Lupini et al.[123,124] identified Bi dopants in Si (Figure 18B); and Okuno et al.[125] visualized single Tm atoms in an AlN host (Figure 18E). In addition, Sato et al.[126] examined the 3D positions of Pr dopants in a ZnO crystal; Allen et al.[127] and Oh et al.[128] imaged individual Au atoms in Si; and Rossell et al.[129] imaged Ba atoms in Ba-doped $SrTiO_3$ nanoparticles. These results demonstrate that ADF-STEM imaging is indeed a reliable method for imaging individual impurity atoms inside crystals, provided proper care in specimen preparation is taken and conditions are favorable (e.g., the type of host, sufficient difference between the atomic numbers of the host crystal and the impurity atom, the sample thickness, etc.).

Aberration correction in the STEM has also allowed microscopes to achieve probe sizes < 1.5 Å at beam energies as low as 60 keV[130] or even 30 keV,[131] resulting in greatly reduced knock-on damage in structures composed of light elements. These new possibilities have been exploited by Krivanek et al.[130] to directly image impurities on the edges of graphene and to image single-layer BN containing C and O impurities with atom-by-atom elemental identification[132] (Figure 18C).

In addition to microscope resolution and beam energy, the visibility of an impurity atom in a crystalline host also depends on specimen parameters: crystal structure, crystal orientation, composition, thickness, and depth of the impurity atom from the beam entry surface. The sensitivity of impurity visibility on specimen parameters is mainly governed by how the incident beam channels through the specimen. In a recent paper, Mittal and Mkhoyan[133] reported a systematic *mutislice* simulation-based study of the critical parameters and conditions of the sample and microscope that influence the visibility of individual impurity atoms in ADF-STEM images based on changes in beam-channeling behavior (Figure 19). Other simulation-based studies on the visibility of impurity atoms with ADF-STEM have also been reported.[118,119,123,134,135] Voyles et al.[119] have examined the effect of the impurity atom position on its visibility for noncorrected STEM probes by using Sb-doped Si crystals and observing a rise and fall in visibility due to beam channeling. Dwyer and Etheridge[135] reported that probes of different sizes channel differently in a crystal and thus have different positions of maximum intensity as they propagate

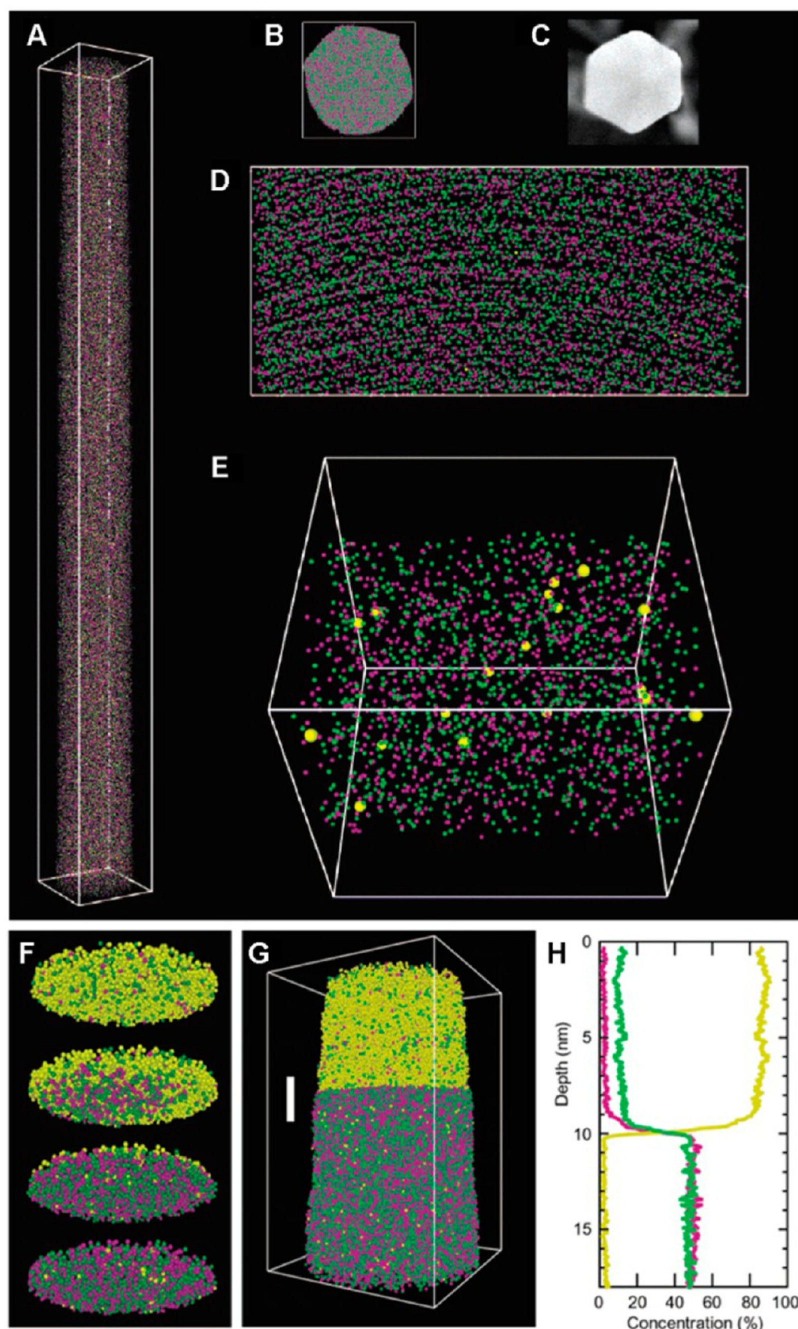

Figure 16. (A) Three-dimensional APT reconstruction of an InAs nanowire. The size of the box is 25 × 25 × 300 nm. In atoms are shown in green, As atoms in violet, and Au atoms in yellow. For clarity, only 5% of the atoms are shown. (B) End-on view of the reconstruction and (C) cross-sectional scanning electron microscope (SEM) image of the nanowire. (D) Magnified view of the reconstruction and (E) a reconstruction with the Au atoms enlarged and only 2% of the In and As atoms shown for clarity. (F−G) APT reconstruction of the interface between the InAs and the Au catalyst on the nanowire tip. The 1-nm-thick slices in (F) correspond to the region marked by the white bar in (G). The size of the box in (G) is 14 × 14 × 23 nm. (H) Concentration profile determined from the reconstruction. Reproduced with permission from ref 102. Copyright 2006 American Chemical Society.

along an atomic column, suggesting that impurity atoms located at certain depths inside a crystal can be detected more easily with a larger probe. Lupini et al.[124] and Xin et al.[120] simulated a defocal series of ADF-STEM images for doped crystals and showed changes in the brightness of the doped column, suggesting that defocusing of the probe might be used to determine the depth of the dopant atom within the specimen.

However, one weakness of ADF-STEM is that it requires that the impurity have a large atomic-number contrast (Z contrast) with the atoms in the host lattice. If this criterion is not satisfied, other methods are needed for dopant detection. One alternative is to combine EELS with ADF-STEM. Such an approach has recently been utilized to determine the composition and local properties of various materials.[136,137] EELS-ADF-STEM also offers several additional advantages for probing dopants buried in semiconductor nanostructures. In particular, while conventional ADF-STEM must detect a minute change in the scattering signal when a dopant atom is

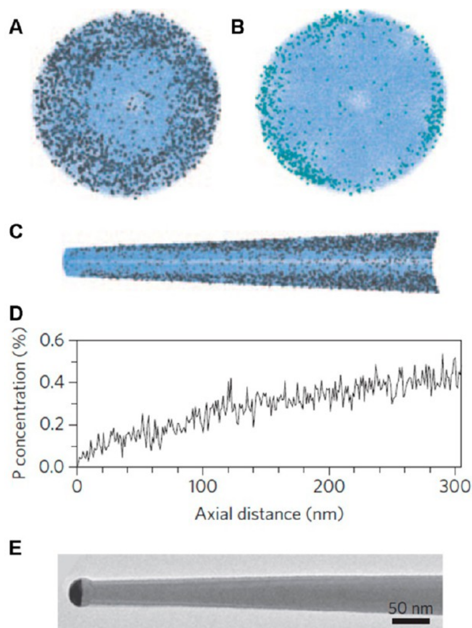

Figure 17. (A–B) End-on view showing the distribution of P (gray), O (blue-green), and Ge (light blue) atoms within a doped Ge nanowire. (C) Side-view APT reconstruction showing the phosphorus-doped shell region of the nanowire. (D) Impurity concentration profile determined from the reconstruction. (E) TEM image of the nanowire reconstructed in (C). Reprinted from ref 104 with permission from Macmillan Publishers Ltd.: Nature Nanotechnology. Copyright 2009 Nature Publishing Group.

present, EELS-ADF-STEM is a zero-background technique. The core-edge EELS signal, which is characteristic of the impurity atom of interest, is either detected or not at any one location on the sample. This advantage has been exploited to detect single atoms in carbon nanostructures (Figure 20A).[138−140] The EELS signal from a single La impurity in crystalline $CaTiO_3$ has also been measured (Figure 20B).[141]

Further, the EELS-ADF-STEM approach has recently been successfully used to detect impurity atoms in doped semiconductor nanocrystals.[142] Namely, as shown in Figure 21, individual Mn atoms were detected in ZnSe quantum dots. Due to low Z-contrast, these dopants are invisible to regular ADF-STEM imaging. However, they are clearly observed with EELS-ADF-STEM (Figure 21B). In this work, Mn was used as a model system because EPR experiments had already shown that the impurity was embedded inside the nanocrystal. However, EELS-ADF-STEM should be broadly applicable to a variety of impurities that meet certain requirements. Namely, they should have a core-level EELS edge with energy less than 1 keV.[130] As previously discussed,[142] this includes elements from Li (Z_{Li} = 2) to Cu (Z_{Cu} = 29) with strong EELS signals for the K- or $L_{2,3}$-edges, elements from Kr (Z_{Kr} = 36) to Ru (Z_{Ru} = 44) with a strong $M_{4,5}$-edge between 80 and 300 eV, and elements from Cs (Z_{Cs} = 55) to Yb (Z_{Yb} = 70) with strong $M_{4,5}$- or $N_{4,5}$-edges. Of course, preventing beam damage in these experiments remains an important issue. Consequently, a high-brightness aberration-corrected electron beam with low accelerating voltage is best suited to these measurements.

VI. OUTLOOK

As research on impurity incorporation in semiconductor nanostructures continues to advance, the ability to image and characterize atomic impurities in nanoscale semiconductors has become increasingly important. Techniques such as in situ TEM currently enable dynamic processes involving atomic impurities to be directly observed and characterized, while techniques such as APT allow impurity distributions to be accurately characterized through three-dimensional atomic

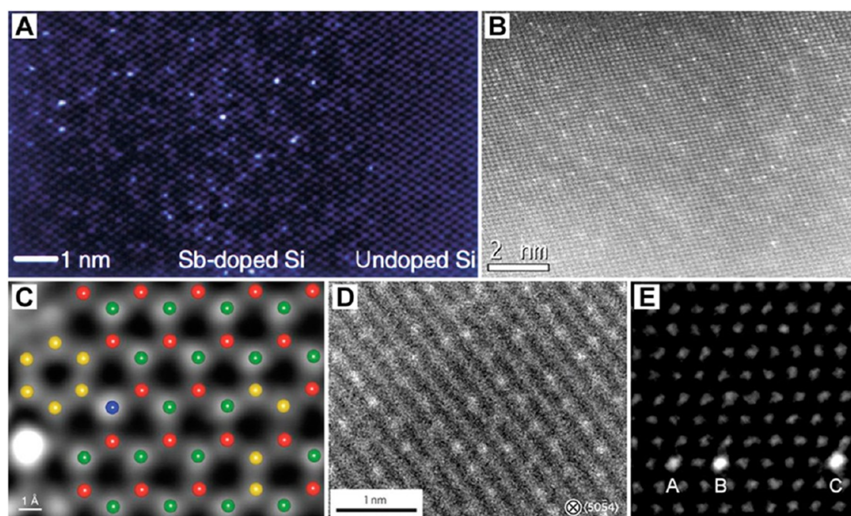

Figure 18. Examples of the use of ADF-STEM imaging to identify dopant atoms (bright spots) inside a crystalline host: (A) An image of a highly Sb-doped Si film grown on an undoped Si substrate. Reprinted from ref 121 with permission from Macmillan Publishers Ltd.: Nature. Copyright 2002 Nature Publishing Group. (B) An image of Si implanted with Bi impurities. Reproduced with permission from ref 124. Copyright 2009 Cambridge University Press. (C) An image of a single BN layer containing O and C impurities. The colors indicate the atom identity as determined by the relative scattering intensities (red, B; yellow, C; green, N; blue, O). Reproduced from ref 132 with permission from Macmillan Publishers Ltd.: Nature. Copyright 2010 Nature Publishing Group. (D) An image of a Y-doped grain boundary in α-Al_2O_3 viewed along the direction perpendicular to the grain boundary. Reprinted from ref 122 with permission from Macmillan Publishers Ltd.: Nature Materials. Copyright 2009 Nature Publishing Group. (E) An image of an AlN crystal containing Tm dopants. Reprinted with permission from ref 125. Copyright 2010 American Institute of Physics.

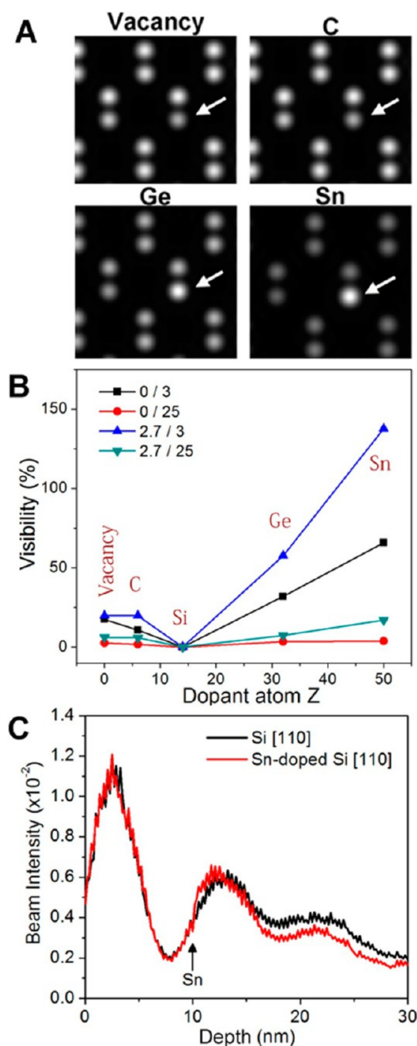

Figure 19. (A) Simulated ADF-STEM images of a Si crystal in the [110] orientation with a single vacancy point defect, as well as with a single C, Ge, and Sn substitutional dopant (the arrow points to the atomic column with the dopant atom). (B) Visibility of the dopant atom as a function of specimen thickness (3 and 25 nm) and depth from the surface (0 and 2.7 nm). (C) Incident beam intensity as it propagates along the Si atomic columns in the [110] direction with and without a single Sn dopant atom. Reprinted with permission from ref 133. Copyright 2011 Elsevier.

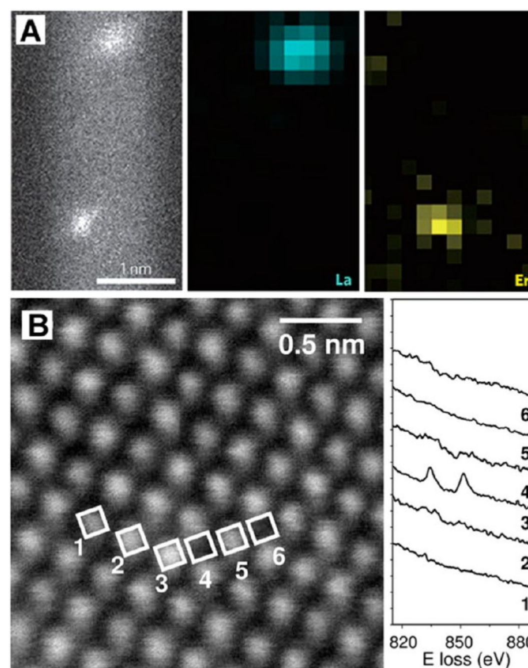

Figure 20. EELS combined with ADF-STEM imaging for spectral identification of single atoms buried in a matrix. (A) Element-selective imaging of single La and Er atoms in a carbon nanotube peapod structure with metallofullerene cages that contain single metal atoms: ADF-STEM image (left) where impurity atoms are visible but elemental identification is not possible, and EELS maps of La (blue) and Er (yellow) $N_{4,5}$-edges (center and right, respectively). Reprinted from ref 139 with permission from Macmillan Publishers Ltd.: Nature Chemistry. Copyright 2009 Nature Publishing Group. (B) ADF-STEM image (left) and EELS signal (right) used for spectroscopic identification of a single La atom in a $CaTiO_3$ perovskite structure. Reprinted with permission from ref 141. Copyright 2004 The American Physical Society.

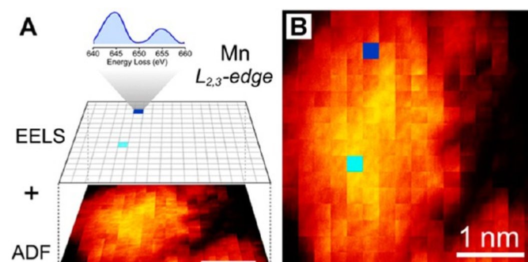

Figure 21. Detection of Mn dopant atoms in a ZnSe nanocrystal using EELS and ADF-STEM: (A) the extracted core-level EELS map (shown as pixels on a grid) for the Mn $L_{2,3}$-edge along with the corresponding ADF-STEM image and (B) overlap of the EELS Mn $L_{2,3}$-edge intensity map and the ADF-STEM image, both shown in (A). Reproduced with permission from ref 142. Copyright 2011 American Chemical Society.

reconstructions. Advanced electron microscopy techniques like ADF-STEM and EELS have demonstrated the ability to detect and characterize individual impurity atoms located within nanoscale semiconductors. Nonetheless, further improvement is needed in each of these techniques. Both in situ TEM and EELS-ADF-STEM will continue to benefit from advances in aberration correction, which help mitigate electron-beam damage by allowing lower accelerating voltages to be used without sacrificing resolution. APT is currently limited by sample preparation requirements, knowledge of how the specimen geometry (and electric field) evolves as the sample is analyzed, and data reconstruction algorithms. Any mechanical weaknesses in the sample can lead to fracture and decrease specimen yield. Therefore, standardized methods for preparing suitable APT specimens from nanomaterials would be extremely useful, along with better reconstruction algorithms, and dynamic information about changes in the shape of the specimen during analysis. It can be argued that advances in detector technology would be beneficial for all three characterization techniques. Faster imaging detectors would enable higher frame rates for in situ TEM experiments, and position-sensitive ion detectors that enable higher detection efficiencies in APT would aid in the accurate compositional analysis of increasingly small nanostructures. Despite the inherent shortcomings that are associated with any technology, in situ TEM, APT, and EELS-ADF-STEM each hold great promise for future

discoveries. As these techniques continue to develop and become more sophisticated and powerful, they are likely to solidify their role as indispensable characterization tools for nanomaterials, facilitating greater understanding of how impurities affect the properties of semiconductor nanostructures.

■ AUTHOR INFORMATION

Corresponding Author

*E-mail: dnorris@ethz.ch.

Notes

The authors declare no competing financial interest.

■ ACKNOWLEDGMENTS

The authors wish to thank Dr. Stephan Gerstl for helpful discussions regarding APT. This work was supported by the Swiss National Science Foundation under Award No. 200021-140617. Additional support was provided by the MRSEC Program of the U.S. National Science Foundation (NSF) under Award No. DMR-0819885. V.C.H. also gratefully acknowledges funding from a Marie Curie ETH postdoctoral fellowship.

■ REFERENCES

(1) Ashcroft, N. W.; Mermin, N. D. *Solid State Physics*; W. B. Saunders: Orlando, 1976.
(2) Klein, D. L.; Roth, R.; Lim, A. K. L.; Alivisatos, A. P.; McEuen, P. L. *Nature* **1997**, *389*, 699−701.
(3) Banin, U.; Cao, Y. W.; Katz, D.; Millo, O. *Nature* **1999**, *400*, 542−544.
(4) Yu, D.; Wang, C. J.; Guyot-Sionnest, P. *Science* **2003**, *300*, 1277−1280.
(5) Norris, D. J.; Bawendi, M. G. *Phys. Rev. B* **1996**, *53*, 16338−16346.
(6) Empedocles, S. A.; Bawendi, M. G. *Acc. Chem. Res.* **1999**, *32*, 389−396.
(7) Nirmal, M.; Brus, L. E. *Acc. Chem. Res.* **1999**, *32*, 407−414.
(8) Smith, D. A.; Holmberg, V. C.; Korgel, B. A. *ACS Nano* **2010**, *4*, 2356−2362.
(9) Goldstein, A. N.; Echer, C. M.; Alivisatos, A. P. *Science* **1992**, *256*, 1425−1427.
(10) Tolbert, S. H.; Alivisatos, A. P. *Science* **1994**, *265*, 373−376.
(11) Chen, C.-C.; Herhold, A. B.; Johnson, C. S.; Alivisatos, A. P. *Science* **1997**, *276*, 398−401.
(12) Jacobs, K.; Zaziski, D.; Scher, E. C.; Herhold, A. B.; Alivisatos, A. P. *Science* **2001**, *293*, 1803−1806.
(13) Holmberg, V. C.; Panthani, M. G.; Korgel, B. A. *Science* **2009**, *326*, 405−407.
(14) Holmberg, V. C.; Collier, K. A.; Korgel, B. A. *Nano Lett.* **2011**, *11*, 3803−3808.
(15) Klimov, V. I. *Nanocrystal Quantum Dots*, 2nd ed.; CRC Press: Boca Raton, 2010.
(16) Norris, D. J.; Efros, A. L.; Erwin, S. C. *Science* **2008**, *319*, 1776−1779.
(17) Koenraad, P. M.; Flatté, M. E. *Nat. Mater.* **2011**, *10*, 91−100.
(18) Bhargava, R. N.; Gallagher, D.; Hong, X.; Nurmikko, A. *Phys. Rev. Lett.* **1994**, *72*, 416−419.
(19) Norris, D. J.; Yao, N.; Charnock, F. T.; Kennedy, T. A. *Nano Lett.* **2001**, *1*, 3−7.
(20) Pradhan, N.; Goorskey, D.; Thessing, J.; Peng, X. *J. Am. Chem. Soc.* **2005**, *127*, 17586−17587.
(21) Viswanatha, R.; Brovelli, S.; Pandey, A.; Crooker, S. A.; Klimov, V. I. *Nano Lett.* **2011**, *11*, 4753−4758.
(22) Sahu, A.; Kang, M. S.; Kompch, A.; Notthoff, C.; Wills, A. W.; Deng, D.; Winterer, M.; Frisbie, C. D.; Norris, D. J. *Nano Lett.* **2012**, *12*, 2587−2594.
(23) Asenov, A.; Brown, R.; Davies, J. H.; Kaya, S.; Slavcheva, G. *IEEE Trans. Electron Devices* **2003**, *50*, 1837−1852.
(24) Yang, C.; Zhong, Z.; Lieber, C. M. *Science* **2005**, *310*, 1304−1307.
(25) Lu, W.; Lieber, C. M. *Nat. Mater.* **2007**, *6*, 841−850.
(26) Ho, J. C.; Yerushalmi, R.; Jacobson, Z. A.; Fan, Z.; Alley, R. L.; Javey, A. *Nat. Mater.* **2008**, *7*, 62−67.
(27) Koren, E.; Hyun, J. K.; Givan, U.; Hemesath, E. R.; Lauhon, L. J.; Rosenwaks, Y. *Nano Lett.* **2011**, *11*, 183−187.
(28) Hoffman, D. M.; Meyer, B. K.; Ekimov, A. I.; Merkulov, I. A.; Efros, Al. L.; Rosen, M.; Couino, G.; Gacoin, T.; Boilot, J. P. *Solid State Commun.* **2000**, *114*, 547−550.
(29) Radovanovic, P. V.; Gamelin, D. R. *J. Am. Chem. Soc.* **2001**, *123*, 12207−12214.
(30) Hanif, K. M.; Meulenberg, R. W.; Strouse, G. F. *J. Am. Chem. Soc.* **2002**, *124*, 11495−11502.
(31) Stowell, C. A.; Wiacek, R. J.; Saunders, A. E.; Korgel, B. A. *Nano Lett.* **2003**, *3*, 1441−1447.
(32) Bussian, D. A.; Crooker, S. A.; Yin, M.; Brynda, M.; Efros, Al. L.; Klimov, V. I. *Nat. Mater.* **2009**, *8*, 35−40.
(33) Beaulac, R.; Schneider, L.; Archer, P. I.; Bacher, G.; Gamelin, D. R. *Science* **2009**, *325*, 973−976.
(34) Efros, Al. L.; Rashba, E. I.; Rosen, M. *Phys. Rev. Lett.* **2001**, *87*, 206601.
(35) Leung, L. K.; Komplin, N. J.; Ellis, A. B.; Tabatabaie, N. *J. Phys. Chem.* **1991**, *95*, 5918−5924.
(36) Son, D. H.; Hughes, S. M.; Yin, Y.; Alivisatos, A. P. *Science* **2004**, *306*, 1009−1012.
(37) Robinson, R. D.; Sadtler, B.; Demchenko, D. O.; Erdonmez, C. K.; Wang, L.-W.; Alivisatos, A. P. *Science* **2007**, *317*, 355−358.
(38) Li, H. B.; Zanella, M.; Genovese, A.; Povia, M.; Falqui, A.; Giannini, C.; Manna, L. *Nano Lett.* **2011**, *11*, 4964−4970.
(39) Wu, Y.; Xiang, J.; Lu, W.; Lieber, C. M. *Nature* **2004**, *430*, 61−65.
(40) Schmitt, A. L.; Higgins, J. M.; Szczech, J. R.; Jin, S. *J. Mater. Chem.* **2010**, *20*, 223−235.
(41) Chan, C. K.; Peng, H.; Liu, G.; McIlwrath, K.; Zhang, X. F.; Huggins, R. A.; Cui, Y. *Nat. Nanotechnol.* **2008**, *3*, 31−35.
(42) Chan, C. K.; Patel, R. N.; O'Connell, M. J.; Korgel, B. A.; Cui, Y. *ACS Nano* **2010**, *4*, 1443−1450.
(43) Chockla, A. M.; Harris, J. T.; Akhavan, V. A.; Bogart, T. D.; Holmberg, V. C.; Steinhagen, C.; Mullins, C. B.; Stevenson, K. J.; Korgel, B. A. *J. Am. Chem. Soc.* **2011**, *133*, 20914−20921.
(44) Chockla, A. M.; Panthani, M. G.; Holmberg, V. C.; Hessel, C. M.; Reid, D. K.; Bogart, T. D.; Harris, J. T.; Mullins, C. B.; Korgel, B. A. *J. Phys. Chem. C* **2012**, *116*, 11917−11923.
(45) Hoeneise, B.; Mead, C. A. *Solid-State Electron.* **1972**, *15*, 819−829.
(46) Bryan, J. D.; Gamelin, D. R. *Prog. Inorg. Chem.* **2005**, *54*, 47−126.
(47) Ekimov, A. I.; Kudryavtsev, I. A.; Ivanov, M. G.; Efros, Al. L. *J. Lumin.* **1990**, *46*, 83−95.
(48) Kennedy, T. A.; Glaser, E. R.; Klein, P. B.; Bhargava, R. N. *Phys. Rev. B* **1995**, *52*, R14356−R14359.
(49) Yang, Y.; Chen, O.; Angerhofer, A.; Cao, Y. C. *J. Am. Chem. Soc.* **2006**, *128*, 12428−12429.
(50) Zu, L.; Wills, A. W.; Kennedy, T. A.; Glaser, E. R.; Norris, D. J. *J. Phys. Chem. C* **2010**, *114*, 21969−21975.
(51) Wills, A. W.; Kang, M. S.; Wentz, K. M.; Hayes, S. E.; Sahu, A.; Gladfelter, W. L.; Norris, D. J. *J. Mater. Chem.* **2012**, *22*, 6335−6342.
(52) Brehm, J. U.; Winterer, M.; Hahn, H. *J. Appl. Phys.* **2006**, *100*, 064311.
(53) Moreau, L. M.; Ha, D.-H.; Bealing, C. R.; Zhang, H.; Hennig, R. G.; Robinson, R. D. *Nano Lett.* **2012**, *12*, 4530−4539.
(54) Mokari, T.; Aharoni, A.; Popov, I.; Banin, U. *Angew. Chem.* **2006**, *45*, 8001−8005.
(55) Wu, Y.; Yang, P. *Adv. Mater.* **2001**, *13*, 520−523.
(56) Banhart, F.; Hernández, E.; Terrones, M. *Phys. Rev. Lett.* **2003**, *90*, 185502.

(57) Gao, Y.; Bando, Y. *Nature* **2002**, *415*, 599.
(58) Sutter, E.; Sutter, P.; Zhu, Y. *Nano Lett.* **2005**, *5*, 2092−2096.
(59) Sun, L.; Banhart, F.; Krasheninnikov, A. V.; Rodríguez-Manzo, J. A.; Terrones, M.; Ajayan, P. M. *Science* **2006**, *312*, 1199−1202.
(60) Sun, L.; Krasheninnikov, A. V.; Ahlgren, T.; Nordlund, K.; Banhart, F. *Phys. Rev. Lett.* **2008**, *101*, 156101.
(61) Kodambaka, S.; Tersoff, J.; Reuter, M. C.; Ross, F. M. *Science* **2007**, *316*, 729−732.
(62) Zheng, H.; Smith, R. K.; Jun, Y.-W.; Kisielowski, C.; Dahmen, U.; Alivisatos, A. P. *Science* **2009**, *324*, 1309−1312.
(63) Yuk, J. M.; Park, J.; Ercius, P.; Kim, K.; Hellebusch, D. J.; Crommie, M. F.; Lee, J. Y.; Zettl, A.; Alivisatos, A. P. *Science* **2012**, *336*, 61−64.
(64) Wen, C.-Y.; Reuter, M. C.; Bruley, J.; Tersoff, J.; Kodambaka, S.; Stach, E. A.; Ross, F. M. *Science* **2009**, *326*, 1247−1250.
(65) Ross, F. M. *Rep. Prog. Phys.* **2010**, *73*, 114501.
(66) Sutter, P. W.; Sutter, E. A. *Nano Lett.* **2007**, *6*, 363−366.
(67) Eswaramoorthy, S. K.; Howe, J. M.; Muralidharan, G. *Science* **2007**, *318*, 1437−1440.
(68) Sutter, E.; Sutter, P. *Nano Lett.* **2008**, *8*, 411−414.
(69) Sutter, E. A.; Sutter, P. W. *ACS Nano* **2010**, *4*, 4943−4947.
(70) Espinosa, H. D.; Bernal, R. A.; Filleter, T. *Small* **2012**, *8*, 3233−3252.
(71) Xiang, B.; Hwang, D. J.; In, J. B.; Ryu, S.-G.; Yoo, J.-H.; Dubon, O.; Minor, A. M.; Grigoropoulos, C. P. *Nano Lett.* **2012**, *12*, 2524−2529.
(72) Williamson, M. J.; Tromp, R. M.; Vereecken, P. M.; Hull, R.; Ross, F. M. *Nat. Mater.* **2003**, *2*, 532−536.
(73) Evans, J. E.; Lungjohann, K. L.; Browning, N. D.; Arslan, I. *Nano Lett.* **2011**, *11*, 2809−2813.
(74) de Jonge, N.; Ross, F. M. *Nat. Nanotechnol.* **2011**, *6*, 695−704.
(75) Yuk, J. M.; Park, J.; Ercius, P.; Kim, K.; Hellebusch, D. J.; Crommie, M. F.; Lee, J. Y.; Zettl, A.; Alivisatos, A. P. *Science* **2012**, *336*, 61−64.
(76) Liao, H.-G.; Cui, L.; Whitelam, S.; Zheng, H. *Science* **2012**, *336*, 1011−1014.
(77) Jin, C. H.; Wang, J. Y.; Chen, Q.; Peng, L.-M. *J. Phys. Chem. B* **2006**, *110*, 5423−5428.
(78) Legros, M.; Dehm, G.; Arzt, E.; Balk, T. J. *Science* **2008**, *319*, 1646−1649.
(79) Chen, Y.; Lin, Y.-C.; Huang, C.-W.; Wang, C.-W.; Chen, L.-J.; Wu, W.-W.; Huang, Y. *Nano Lett.* **2012**, *12*, 3115−3120.
(80) Lin, Y.-C.; Chen, Y.; Xu, D.; Huang, Y. *Nano Lett.* **2010**, *10*, 4721−4726.
(81) Dellas, N. S.; Schuh, C. J.; Mohney, S. E. *J. Mater. Sci.* **2012**, *47*, 6189−6205.
(82) Huang, J. Y.; Zhong, L.; Wang, C. M.; Sullivan, J. P.; Xu, W.; Zhang, L. Q.; Mao, S. X.; Hudak, N. S.; Liu, X. H.; Subramanian, A.; Fan, H.; Qi, L.; Kushima, A.; Li, J. *Science* **2010**, *330*, 1515−1520.
(83) Liu, X. H.; Zhang, L. Q.; Zhong, L.; Liu, Y.; Zheng, H.; Wang, J. W.; Cho, J.-H.; Dayeh, S. A.; Picraux, S. T.; Sullivan, J. P.; Mao, S. X.; Ye, Z. Z.; Huang, J. Y. *Nano Lett.* **2011**, *11*, 2251−2258.
(84) Liu, X. H.; Huang, J. Y. *Energy Environ. Sci.* **2011**, *4*, 3844−3860.
(85) Liu, X. H.; Liu, Y.; Kushima, A.; Zhang, S.; Zhu, T.; Li, J.; Huang, J. Y. *Adv. Energy Mater.* **2012**, *2*, 722−741.
(86) Zheng, H.; Rivest, J. B.; Miller, T. A.; Sadtler, B.; Lindenberg, A.; Toney, M. F.; Wang, L.-W.; Kisielowski, C.; Alivisatos, A. P. *Science* **2011**, *333*, 206−209.
(87) Nam, S.-W.; Chung, H.-S.; Lo, Y. C.; Qi, L.; Li, J.; Lu, Y.; Johnson, A. T. C.; Jung, Y.; Nukala, P.; Agarwal, R. *Science* **2012**, *336*, 1561−1566.
(88) Williams, D. B.; Carter, C. B. Inelastic Scattering and Beam Damage. In *Transmission Electron Microscopy: A Textbook for Materials Science*, 2nd ed.; Springer Science: New York, 2009; Chapter 4, pp 64−68.
(89) Loferski, J. J.; Rappaport, P. *Phys. Rev.* **1958**, *111*, 432−439.
(90) Volin, T. E.; Lie, K. H.; Balluffi, R. W. *Acta Metall.* **1971**, *19*, 263−274.
(91) Fujikawa, S.-I.; Hirano, K.-I.; Fukushima, Y. *Metall. Trans. A* **1978**, *9*, 1811−1815.
(92) Müller, E. W. Field Ionization and Field Ion Microscopy. In *Advances in Electronics and Electron Physics*; Marton, L. M., Marton, C. M., Eds.; Academic Press: 1960; Vol. *13*, pp 83−179.
(93) Müller, E. W.; Panitz, J. A.; McLane, S. B. *Rev. Sci. Instrum.* **1968**, *39*, 83−86.
(94) Kelly, T. F.; Gribb, A. A. *Microsc. Today* **2003**, *11*, 8−12.
(95) Miller, M. K. *Atom Probe Tomography: Analysis at the Atomic Level*, 1st ed.; Kluwer Academic/Plenum Publishers: New York, NY, 2000.
(96) Kelly, T. F.; Gribb, T. T.; Olson, J. D.; Martens, R. L.; Shepard, J. D.; Wiener, S. A.; Kunicki, T. C.; Ulfig, R. M.; Lenz, D. R.; Strennen, E. M.; Oltman, E.; Bunton, J. H.; Strait, D. R. *Microsc. Microanal.* **2004**, *10*, 373−383.
(97) Kelly, T. F.; Miller, M. K. *Rev. Sci. Instrum.* **2007**, *78*, 031101.
(98) Gault, B.; Moody, M. P.; De Geuser, F.; La Fontaine, A.; Stephenson, L. T.; Haley, D.; Ringer, S. P. *Microsc. Microanal.* **2010**, *16*, 99−110.
(99) Shariq, A.; Mutas, S.; Wedderhoff, K.; Klein, C.; Hortenbach, H.; Teichert, S.; Kücher, P.; Gerstl, S. S. A. *Ultramicroscopy* **2009**, *109*, 472−479.
(100) Miller, M. K.; Russell, K. F.; Thompson, K.; Alvis, R.; Larson, D. J. *Microsc. Microanal.* **2007**, *13*, 428−436.
(101) Kelly, T. F.; Larson, D. J.; Thompson, K.; Alvis, R. L.; Bunton, J. H.; Olson, J. D.; Gorman, B. P. *Annu. Rev. Mater. Res.* **2007**, *37*, 681−727.
(102) Perea, D. E.; Allen, J. E.; May, S. J.; Wessels, B. W.; Seidman, D. N.; Lauhon, L. J. *Nano Lett.* **2006**, *6*, 181−185.
(103) Perea, D. E.; Wijaya, E.; Lensch-Falk, J. L.; Hemesath, E. R.; Lauhon, L. J. *J. Solid State Chem.* **2008**, *181*, 1642−1649.
(104) Perea, D. E.; Hemesath, E. R.; Schwalbach, E. J.; Lensch-Falk, J. L.; Voorhees, P. W.; Lauhon, L. J. *Nat. Nanotechnol.* **2009**, *4*, 315−319.
(105) Schlitz, R. A.; Perea, D. E.; Lensch-Falk, J. L.; Hemesath, E. R.; Lauhon, L. J. *Appl. Phys. Lett.* **2009**, *95*, 162101.
(106) Connell, J. G.; Yoon, K.; Perea, D. E.; Schwalbach, E. J.; Voorhees, P. W.; Lauhon, L. J. *Nano Lett.* **2012**, *13*, 199−206.
(107) Crewe, A. V. *Science* **1966**, *154*, 729−738.
(108) Crewe, A. V.; Wall, J.; Langmore, J. *Science* **1970**, *168*, 1338−1340.
(109) Pennycook, S. J.; Boatner, L. A. *Nature* **1988**, *336*, 565−567.
(110) Treacy, M. M. J. *Microsc. Microanal.* **2011**, *17*, 847−858.
(111) Batson, P. E.; Dellby, N.; Krivanek, O. L. *Nature* **2002**, *418*, 617−620.
(112) Muller, D. A.; Singh, D. J.; Silcox, J. *Phys. Rev. B* **1998**, *57*, 8181−8202.
(113) Bosman, M.; Keast, V. J.; García-Muñoz, J. L.; D'Alfonso, A. J.; Findlay, S. D.; Allen, L. J. *Phys. Rev. Lett.* **2007**, *99*, 086102.
(114) Kimoto, K.; Asaka, T.; Nagai, T.; Saito, M.; Matsui, Y.; Ishizuka, K. *Nature* **2007**, *450*, 702−704.
(115) Muller, D. A.; Kourkoutis, L. F.; Murfitt, M.; Song, J. H.; Hwang, H. Y.; Silcox, J.; Dellby, N.; Krivanek, O. L. *Science* **2008**, *319*, 1073−1076.
(116) Meyer, J. C.; Girit, C. O.; Crommie, M. F.; Zettl, A. *Nature* **2008**, *454*, 319−322.
(117) Fertig, J.; Rose, H. *Optik* **1981**, *59*, 407−429.
(118) Loane, R. F.; Kirkland, E. J.; Silcox, J. *Acta Crystallogr.* **1988**, *A44*, 912−927.
(119) Voyles, P. M.; Muller, D. A.; Kirkland, E. J. *Microsc. Microanal.* **2004**, *10*, 291−300.
(120) Xin, H. L.; Intaraprasonk, V.; Muller, D. A. *Appl. Phys. Lett.* **2008**, *92*, 013125.
(121) Voyles, P. M.; Muller, D. A.; Grazul, J. L.; Citrin, P. H.; Gossmann, H.-J. L. *Nature* **2002**, *416*, 826−829.
(122) Shibata, N.; Findlay, S. D.; Azuma, S.; Mizoguchi, T.; Yamamoto, T.; Ikuhara, Y. *Nat. Mater.* **2009**, *8*, 654−658.
(123) Lupini, A. R.; Pennycook, S. J. *Ultramicroscopy* **2003**, *96*, 313−322.

(124) Lupini, A. R.; Borisevich, A. Y.; Idrobo, J. C.; Christen, H. M.; Biegalski, M.; Pennycook, S. J. *Microsc. Microanal.* **2009**, *15*, 441−453.
(125) Okuno, H.; Rouvière, J.-L.; Jouneau, P.-H.; Bayle-Guillemaud, P.; Daudin, B. *Appl. Phys. Lett.* **2010**, *96*, 251908.
(126) Sato, Y.; Mizoguchi, T.; Shibata, N.; Yamamoto, T.; Hirayama, T.; Ikuhara, Y. *Phys. Rev. B* **2009**, *80*, 094114.
(127) Allen, J. E.; Hemesath, E. R.; Perea, D. E.; Lensch-Falk, J. L.; Li, Z. Y.; Yin, F.; Gass, M. H.; Wang, P.; Bleloch, A. L.; Palmer, R. E.; Lauhon, L. J. *Nat. Nanotechnol.* **2008**, *3*, 168−173.
(128) Oh, S. H.; van Benthem, K.; Molina, S. I.; Borisevich, A. Y.; Luo, W.; Werner, P.; Zakharov, N. D.; Kumar, D.; Pantelides, S. T.; Pennycook, S. J. *Nano Lett.* **2008**, *8*, 1016−1019.
(129) Rossell, M. D.; Ramasse, Q. M.; Findlay, S. D.; Rechberger, F.; Erni, R.; Niederberger, M. *ACS Nano* **2012**, *6*, 7077−7083.
(130) Krivanek, O. L.; Dellby, N.; Murfitt, M. F.; Chisholm, M. F.; Pennycook, T. J.; Suenaga, K.; Nicolosi, V. *Ultramicroscopy* **2010**, *110*, 935−945.
(131) Suenaga, K.; Iizumi, Y.; Okazaki, T. *Eur. Phys. J. Appl. Phys.* **2011**, *54*, 33508.
(132) Krivanek, O. L.; Chisholm, M. F.; Nicolosi, V.; Pennycook, T. J.; Corbin, G. J.; Dellby, N.; Murfitt, M. F.; Own, C. S.; Szilagyi, Z. S.; Oxley, M. P.; Pantelides, S. T.; Pennycook, S. J. *Nature* **2010**, *464*, 571−574.
(133) Mittal, A.; Mkhoyan, K. A. *Ultramicroscopy* **2011**, *111*, 1101−1110.
(134) Vanfleet, R. R.; Robertson, M.; McKay, M.; Silcox, J. *AIP Conf. Proc.* **1998**, *449*, 901−905.
(135) Dwyer, C.; Etheridge, J. *Ultramicroscopy* **2003**, *96*, 343−360.
(136) Daniels, J.; Festenberg, C. V.; Raether, H.; Zeppenfeld, K. Optical Constants of Solids by Electron Spectroscopy. In *Springer Tracts in Modern Physics*; Hohler, G., Ed.; Springer-Verlag: Berlin, 1970; Vol. *54*, pp 77−135.
(137) Egerton, R. F. *Electron Energy-Loss Spectroscopy in the Electron Microscope*, 3rd ed.; Springer: New York, 2011.
(138) Suenaga, K.; Tencé, M.; Mory, C.; Colliex, C.; Kato, H.; Okazaki, T.; Shinohara, H.; Hirahara, K.; Bandow, S.; Iijima, S. *Science* **2000**, *290*, 2280−2282.
(139) Suenaga, K.; Sato, Y.; Liu, Z.; Kataura, H.; Okazaki, T.; Kimoto, K.; Sawada, H.; Sasaki, T.; Omoto, K.; Tomita, T.; Kaneyama, T.; Kondo, Y. *Nat. Chem.* **2009**, *1*, 415−418.
(140) Suenaga, K.; Koshino, M. *Nature* **2010**, *468*, 1088−1090.
(141) Varela, M.; Findlay, S. D.; Lupini, A. R.; Christen, H. M.; Borisevich, A. Y.; Dellby, N.; Krivanek, O. L.; Nellist, P. D.; Oxley, M. P.; Allen, L. J.; Pennycook, S. J. *Phys. Rev. Lett.* **2004**, *92*, 095502.
(142) Gunawan, A. A.; Mkhoyan, K. A.; Wills, A. W.; Thomas, M. G.; Norris, D. J. *Nano Lett.* **2011**, *11*, 5553−5557.